PROBING III-V SEMICONDUCTOR HETEROSTRUCTURES USING TIME RESOLVED PUMP-PROBE TECHNIQUES

By

Jerome Keith Miller

Dissertation

Submitted to the Faculty of the

Graduate School of Vanderbilt University

in partial fulfillment of the requirements

for the degree of

DOCTOR OF PHILOSOPHY

in

Physics

December, 2006

Nashville, Tennessee

Approved:

Professor Norman H. Tolk

Professor Royal G. Albridge

Professor Steven E. Csorna

Professor Thomas W. Kephart

Professor Ronald D. Schrimpf

To my parents,

my wife,

and my daughter

for their love, support, and sacrifice.

ACKNOWLEDGEMENTS

First I would like to express my gratitude to my advisor, Professor Norman Tolk, for giving me the opportunity to be a part of his research group. I would also like to thank all of the members of my Ph.D. committee, Professor Royal Albridge, Professor Steven Csorna, Professor Tom Kephart, and Professor Ron Schrimpf, for their helpful comments, suggestions, and discussions.

I thank all of the past and present members of the CMASS group, especially Dr. Ying Xu, Dr. Robert Pasternak, Dr. Yelena White, Jingbo Qi, Xiong Lu, Dr. Nageswara Sunkaranam, Travis Wade, and Charles McMillan. All of these members contributed to my success.

I would also like to thank some of the staff at Vanderbilt University. If it wasn't for dedicated people like Jane Fall, Donald Pickert, John Fellenstein, and Bob Patchin, my time at Vanderbilt University would not have been as enjoyable.

I would like to thank my parents, Paul and Joyce, for teaching me at a young age to do well in school and to, above all else, keep my integrity. I also want to thank my daughter, Ella "Bella", for her love and sacrifice during the past two years. Even though she is so young, she taught me that sometimes you need to slow down and enjoy life, because we will never get this time back. Finally, I want to express my greatest appreciation to my wife, Dianna, for her never-ending love, support and sacrifice. This would not be possible without her.

TABLE OF CONTENTS

LIST OF TABLES

LIST OF FIGURES

CHAPTER I

INTRODUCTION

Over the past few years there has been considerable interest in exploring the fundamental limits of semiconductor device operation by investigating at a very basic level the underlying fast nanoscopic processes which occur on a picosecond or even a femtosecond time scale. Momentum and energy relaxation processes involved in carrier-carrier scattering, intervalley and intravalley scattering, optical phonon scattering, and carrier diffusion, have been treated. Research on ultra-fast dynamics has become a strategic field both in basic research and from a technological point of view. Developments in ultra-fast laser physics now allow the study of the interaction processes of nonequilibrium carriers in a semiconductor,[1,2] which occur at a very early time and are directly related to the microscopic details of the coupling mechanisms. Therefore time-resolved laser spectroscopy has become an essential tool in modern semiconductor physics. The development of such optical techniques as pump-probe experiments has enabled the study of both carrier dynamics as well as vibrational dynamics with temporal resolution limited only by the laser pulse itself.[2]

This dissertation will present measurements taken on a unique experimental configuration that can monitor two separate signals during a given experimental run. One of these channels measures the second harmonic generation (SHG) that is produced from the sample. SHG is a versatile second order probe of buried semiconductor interfaces and is known to be extremely sensitive to electric fields occurring at surfaces and

interfaces.[3] The second channel measures differential linear reflectivity. The differential reflectivity not only gives information about the carrier dynamics in bulk semiconductors, but it has been shown to give information about phonon dynamics as well. Even though both signals can be measured simultaneously, this thesis will focus mainly on the phonon dynamics arising from differential reflectivity measurements.

Chapter II will describe the material properties of GaAs. This includes the energy band structure, some important crystal defects found in GaAs, and the affects of temperature on the bandgap energy. This background information is given to lay the ground work for understanding the experimental data that will be presented in later chapters.

Chapter III will give the theory of Second-Harmonic Generation (SHG) and specifically Electric Field Induced Second Harmonic (EFISH) Generation. In the experimental systems that are examined, there is a time independent contribution to the EFISH signal due to the noncentrosymetric nature of the materials. More importantly, there is a time dependent contribution that arises due to the creation of interfacial electric fields.

Chapter IV will describe the experimental configuration of the experiments. This includes the Ti:Sapphire laser and the pump-probe technique. Using the well known pump-probe approach, we are able to probe the relaxation of carriers and phonons on a femtosecond time scale, limited only by the pulse width of the laser we are using.

A general description of the carrier relaxation in semiconductors is given in Chapter V. Information on how energetic electron-hole pairs transfer their energy to the lattice to produce a strain wave that is refered to as a Coherent Longitudinal Acoustic

Phonon (CLAP) wave will be discussed. Using a pump-probe configuration, the propagation of the CLAP wave can be monitored and modeled using a damped harmonic model which is developed in this chapter.

In Chapter VI we report time resolved pump-probe SHG measurements on GaSb/GaAs and InAs/GaSb/GaAs. The ability of SHG to measure electric fields at the interfaces makes it a unique tool to probe the carrier dynamics in these samples since photoexcited electrons and holes move to separate layers. These measurements show a complicated evolution of the interfacial fields originating from the redistribution of carriers between the interfaces.

In Chapter VII we report the use of the CLAP wave technique to probe different materials. Specifically, the CLAP wave will be created in a thin GaSb layer and then propagate into the GaAs substrate. These measurements show oscillations due to interference between the probe beam being reflected from the surface and from the CLAP wave. This systematic study of the GaSb/GaAs system will show (1) a linear behavior of the period with the wavelength of the probe beam, (2) a peak in the amplitude of the oscillations around the bandgap of GaAs which is due to the change in the dielectric function around the bandgap in GaAs, and (3) a new way to measure the bandgap of semiconductors by looking at the damping time of the oscillations as a function of the wavelength of the probe beam.

Also, in Chapter VII it will be shown that CLAP waves can be produced in aluminum and germanium, which allows the possible integration of the CLAP wave technique to modern silicon technology. Also, this technique is applied to probing layers

that are buried in GaAs. The CLAP wave technique is shown to be a new, non-invasive tool for measuring layer thickness as a function of depth.

The final section in Chapter VII shows the construction of a simple model that arises from the idea that these oscillations are due to the interference between the reflection from the surface and from the CLAP wave. This model satisfactorily characterizes our experimental data and exhibits two important features: (1) the amplitude reduction and (2) the phase change at the buried layer. The first feature is due to the probe light being absorbed in this buried layer and the second feature is due to the difference in the index of refraction and the longitudinal sound velocity going from the surrounding material, typically GaAs, to the buried layer.

CHAPTER II

GaAs MATERIAL PROPERTIES

Introduction

GaAs is a III-V compound semiconductor composed of the element gallium (Ga) from column III and the element arsenic (As) from column V of the periodic table. GaAs was first fabricated by Goldschmidt and reported in 1929.[4] The first investigations of the electronic properties of III-V compounds did not appear until 1952.[5]

The GaAs crystal is composed of two sublattices, each face centered cubic (fcc) and offset with respect to each other by one quarter the diagonal of the fcc cube. This crystal configuration is known as cubic sphalerite or zinc blende. Figure 2.1 shows a unit cube for GaAs[6] and Appendix A shows a listing of some of the general material characteristics and properties.

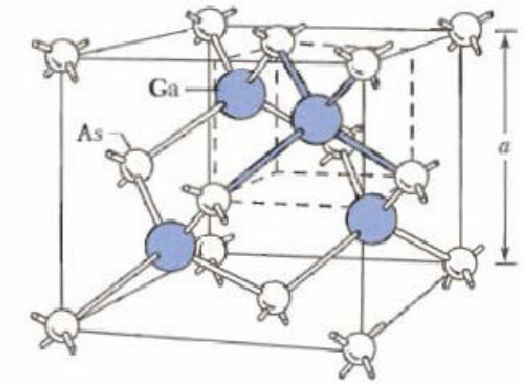

Figure 2.1. Unit cube of GaAs crystal lattice.

Energy Band Structure

Electrons in isolated atoms can have only certain discrete energy values as determined by the laws of quantum mechanics. As these isolated atoms are brought together to form a crystal, the electrons become restricted not to single energy levels, but rather to ranges of allowed energies, or bands, two of which are the valence and conduction bands (Figure 2.2). These two bands are separated by an energy bandgap, which is a very important characteristic of the semiconductor material. At zero Kelvin, all the electrons are confined to the valence band and the material is a perfect insulator. Above zero Kelvin, some electrons may have sufficient thermal energy to make a transition to the conduction band where they are free to move and conduct current through the crystal. The probability of an electron having enough energy to make the transition is given by the Fermi distribution function. The Fermi level shown in Figure 2.2 is the energy level at which the probability function is equal to one half. For pure semiconductors, the Fermi level is approximately in the center of the bandgap. Note, no electron actually has an energy E_F, since they are not permitted to exist at energies in the

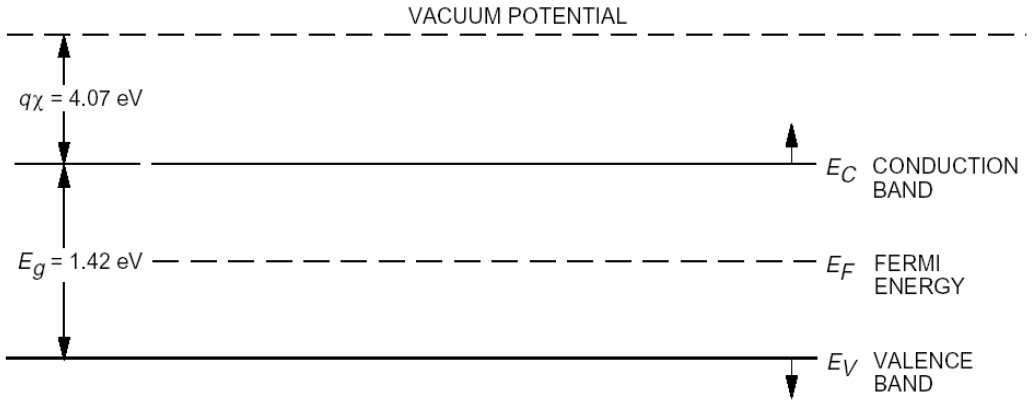

Figure 2.2. Energy band diagram for GaAs.

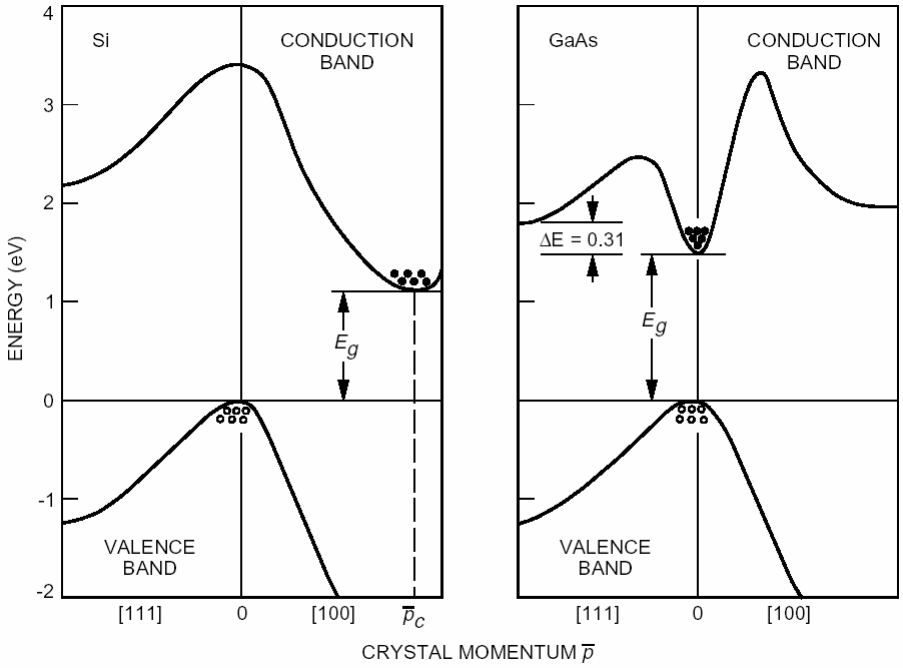

Figure 2.3. Energy band structures of Si and GaAs.[6]

bandgap. The amount of energy required for an electron to move from the valence band to the conduction band (energy bandgap) depends on temperature, the semiconductor material, and the material's purity and doping profile. For undoped GaAs, the energy bandgap at room temperature is 1.42 eV. The energy band diagram is usually referenced to a potential called the vacuum potential. The electron affinity, qc, is the energy required to remove an electron from the bottom of the conduction band to the vacuum potential. For GaAs, qc is approximately 4.07 eV.[6,7]

GaAs is a direct bandgap semiconductor, which means that the minimum of the conduction band is directly over the maximum of the valence band (Figure 2.3). Transitions between the valence band and the conduction band require only a change in energy, and no change in momentum, unlike indirect bandgap semiconductors such as

silicon (Si). This property makes GaAs a very useful material for the manufacture of light emitting diodes and semiconductor lasers, since a photon is emitted when an electron changes energy levels from the conduction band to the valance band. Alternatively, an incident photon can excite an electron from the valence band to the conduction band, allowing GaAs to be used in photo detectors.

Crystal Defects

No semiconductor crystalline material is perfect, and GaAs crystals, in spite of the efforts to control crystal growth, contain a number of crystal defects, dislocations, and impurities. These defects can have either desirable or undesirable effects on the electronic properties of GaAs. The natures of these defects and the observed effects are determined by the method of their incorporation into the material and the general growth conditions.

Localized defects of atomic dimensions, called point defects, can occur in an otherwise perfect crystal lattice.[8] These point defects can include vacancies, interstitials, misplaced atoms, intentionally introduced dopant impurities, and impurities introduced inadvertently during the material growth process. The study of point defects is important because of the effects these defects have on the electronic properties of the material and the strong relationship between diffusion and the number and type of defects in the crystalline material. The electrical properties of a semiconductor can be manipulated by the deliberate insertion of chemical defects (impurities) into the material during the growth process steps. However, intrinsic defects present in the material also play an important role in the electronic behavior of GaAs.

Many intrinsic defects are observed in GaAs. The concentration and effect of these defects are determined by the manner in which the material is grown. Intrinsic defects in GaAs include arsenic and gallium vacancies, their concentration being determined by the overpressure of arsenic during processing. The electronic behavior of these vacancy defects has been observed to be neutral[9], deep donor-like, and deep acceptor-like[10].

An important defect in GaAs called EL2 is present in material grown from an arsenic rich melt. This defect is thought to be an arsenic antisite defect (arsenic on a gallium site).[8] It is donor-like in character and is located at the middle of the energy gap[11]. It is thermally very stable, can withstand processing temperatures up to 900°C, and acts as an electron trap. The importance of this defect lies in its ability to convert p-type GaAs to semi-insulating material, and its thermal stability.

A dislocation is a one-dimensional array of point defects in an otherwise perfect crystal. It occurs when the crystal is subjected to stresses in excess of the elastic limit of the material. Dislocations interact with chemical and other point defects. This interaction exists between the localized impurity atoms and the strain field in the vicinity of the dislocations. The presence of a dislocation is usually associated with an enhanced rate of impurity diffusion leading to the formation of diffusion pipes. This effect translates to the introduction of trapping states in the bandgap, altering the etching properties of the wafer and most importantly, altering the electrical properties of the devices. Studies have shown detrimental effects of dislocations and dislocation densities on the source drain current and threshold voltage of field-effect transistors (FETs)[12,13], carrier concentration, and sheet resistance[14].

Chemical point defects (doping impurities) can be introduced to the crystalline material either deliberately or inadvertently during processing. Dopants are classified as either donors or acceptors. A donor has one more electron than the atom it is replacing in the crystal. This extra electron is easily removed or donated to the conduction band. An acceptor, on the other hand, has one less electron than the atom it is replacing. Thus, an acceptor can easily capture an electron and contribute to the conductivity of the sample by introducing holes, which are positively charged. Regardless of the type or character of the impurity, the electrical properties of the semiconductor are altered.

Figure 2.4 shows the energy band diagram of Figure 2.2 with the addition of impurities. Shallow donor or acceptor impurities have energy levels within a few times the thermal energy kT of the conduction and valence band, respectively.[15] Since the energy required for an electron to transition from these impurity energy levels to the nearest band edge is very small, they are typically nearly fully ionized at room temperature. The Fermi level shifts from the band center towards the impurity levels to

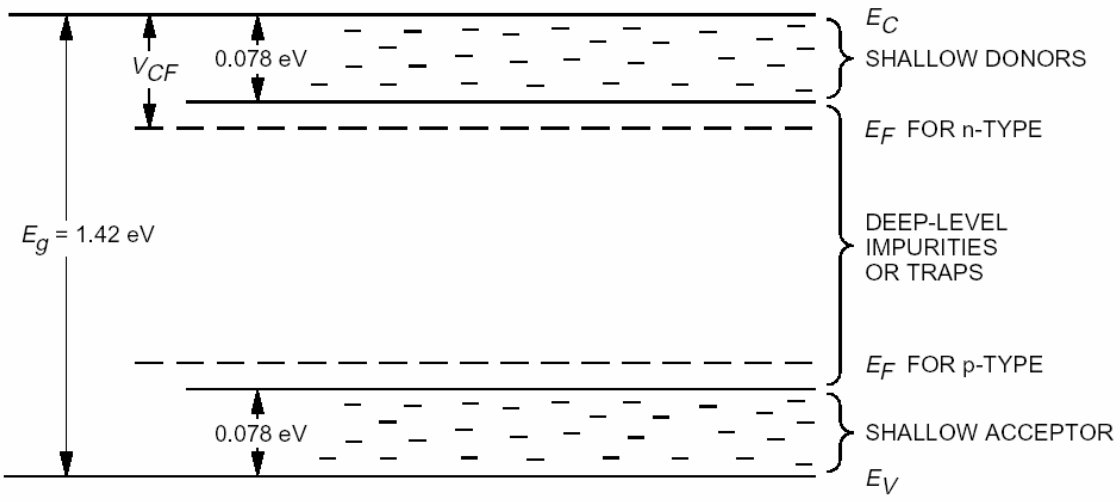

Figure 2.4. Energy band diagram of GaAs with impurities at room temperature.

reflect this. In other words, for donor impurities, the Fermi level shifts towards the conduction band, and V_{CF} decreases as the donor doping concentration increases. A similar description can be made of acceptor impurities. It is these shallow impurities that are used for doping purposes. Impurities with energies in the center of the bandgap are called deep impurities. Deep impurities can degrade device performance by reducing the carrier lifetime.

Both impurity types, deep and shallow, are present in GaAs in the form of complexes with gallium or arsenic. One of the most common is silicon. This group IV element can be used to give either p-type GaAs by incorporating it at low temperatures, or n-type GaAs by processing it at high temperatures. Another group IV element, carbon, is also used extensively to provide p-type GaAs. Chromium (Cr) behaves as an acceptor, with an impurity level close to the center of the energy gap. This property makes it very useful for counterdoping n-type GaAs to make it semi-insulating. Other elements such as copper, oxygen, selenium, and tin are also used in GaAs processing to provide the desired n- or p-like behavior.

Bandgap Temperature Dependence

The energy bandgap of semiconductors tends to decrease as the temperature is increased. This behavior can be better understood if one considers that the interatomic spacing increases when the amplitude of the atomic vibrations increases due to the

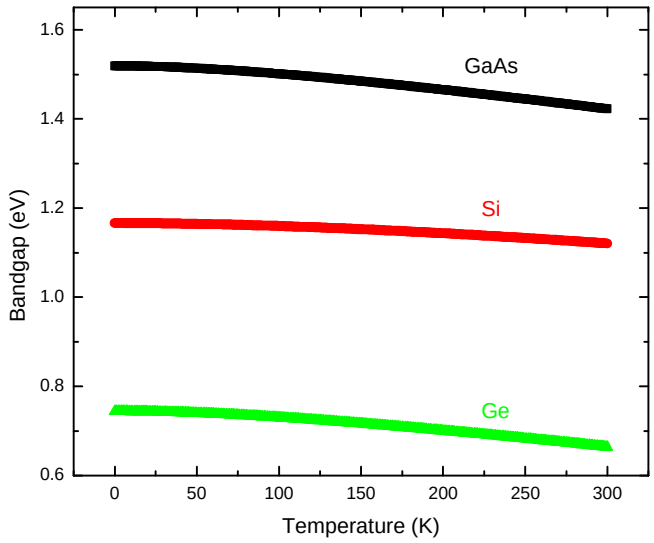

Figure 2.5. Temperature dependence of the Bandgap of GaAs (black), Si (red), and Ge (green).

increased thermal energy. This effect is quantified by the linear expansion coefficient of a material. An increased interatomic spacing decreases the potential seen by the electrons in the material, which in turn reduces the size of the energy bandgap. A direct modulation of the interatomic distance, for example, applying high compressive (tensile) stress, also causes an increase (decrease) of the bandgap.

The temperature dependence of the bandgap of GaAs has been measured with great accuracy by Sell et al.[16,17] and by Panish and Casey[18]. These results were used by Thurmond[19] to determine the coefficients E_0, a, and b of the Varshni equation[20],

$$E_g = E_0 - \frac{aT^2}{(T+b)} \qquad 2.1$$

Table 2.1. Varshni coefficients for Germanium, Silicon, and GaAs.

	Germanium	**Silicon**	**GaAs**
$E_g(0)$ [eV]	0.7437	1.166	1.519
α [eV/K]	4.77×10^{-4}	4.73×10^{-4}	5.41×10^{-4}
β [K]	235	636	204

where E_g is the bandgap energy and T is the temperature. This equation describes the temperature dependence of bandgaps of semiconductors. These fitting parameters are listed for germanium, silicon and gallium arsenide in Table 2.1.

Figure 2.5 shows the behavior of Eq. (2.1) using the Varshni coefficients from Table 2.1 for GaAs. Also included in Figure 4 is the temperature dependence of the bandgaps for Si and Ge for comparison.

This dissertation is comprised of measurements preformed on III-V semiconductor heterostructures. These samples typically have layers of GaAs grown by molecular beam epitaxy (MBE) on a GaAs substrate. To fully understand the results of the experimental data, one needs a basic understanding of the background information presented above. This chapter lays the ground work for understanding the results that are presented in this dissertation.

CHAPTER III

SECOND HARMONIC GENERATION

Nonlinear optics is the study of the interaction of intense light with matter[21]. Typically, only laser light is sufficiently intense to modify the optical properties of a material system. Nonlinear optical phenomena are called nonlinear because they occur when the response of a material system to an applied optical field depends in a nonlinear manner upon the strength of the optical field. An example of a nonlinear response is second-harmonic generation (SHG). SHG occurs as a result of the part of the atomic response that depends quadratically on the strength of the applied optical field. Therefore, the intensity of the generated second harmonic light tends to increase as the square of the intensity of the applied laser light.

A second-harmonic generation process can be illustrated in Figure 3.1 (a). According to this illustration, two photons with the same frequency w when propagating through an appropriate nonlinear medium, can mix together giving rise to photons with twice the incident frequency $2w$.[22] In the classical picture, light propagation is described in terms of coherent emission by harmonic electric dipoles, which have been set to oscillate by the light itself. In the nonlinear regime, if the assumption is made that the oscillation amplitudes of the electronic oscillators are large then the oscillations become strongly anharmonic at these high excitation intensities. Under this assumption, the emitting dipoles can radiate energy at frequencies which are integer multiples of the original frequency.

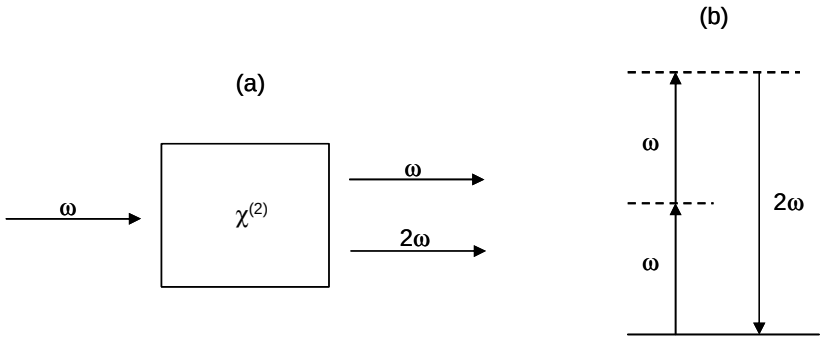

Figure 3.1. (a) Geometry of second-harmonic generation. (b) Energy- level diagram describing second-harmonic generation.

Second-harmonic generation can also be visualized by considering the interaction in terms of the exchange of photons between the various frequency components of the field. According to this picture, which is illustrated in Figure 3.1 (b), the two photons of frequency w are destroyed and a photon of frequency $2w$ is simultaneously created in a single quantum-mechanical process. The solid line represents the atomic ground state, and the dashed lines represent what are known as virtual levels.

Theory of Second-Harmonic Generation

In the case of conventional (linear) optics, the induced polarization (or dipole moment per unit volume) depends linearly upon the electric field strength according to the equation

$$P(t) = c^{(1)}E(t) \qquad 3.1$$

where $c^{(1)}$ is known as the linear susceptibility. This describes the magnitude of the optical response of the material under investigation. In nonlinear optics, the nonlinear response can be described by expressing the polarization $P(t)$ as a power series in the field strength $E(t)$ as

$$P(t) = c^{(1)}E(t) + c^{(2)}E^2(t) + c^{(3)}E^3(t) + ... \qquad 3.2$$

where $E(t) = Ee^{-iwt} + c.c.$ represents the electric field strength and $c^{(i)}$, the i-th order susceptibility tensor, describes the magnitude of the optical response of the system. If only the second-order case is examined, according to Eq. (3.2), the polarization becomes

$$P^{(2)}(t) = c^{(2)}E^2(t) \qquad 3.3$$

or

$$P^{(2)}(t) = 2c^{(2)}EE^* + (c^{(2)}E^2e^{-2iwt} + c.c.). \qquad 3.4$$

The second-order polarization consists of two terms. The first term gives a contribution at zero frequency that leads to a process known as optical rectification in which a static electric field is created within the nonlinear crystal. The second term is a contribution at

frequency $2w$ which can lead to the generation of radiation at the second-harmonic frequency.

In SHG, the components of the second-order susceptibility tensor are defined as proportionality constants relating the second-order polarization to the product of the field amplitudes according to

$$P_i(2w) = \sum_{jk} c_{ijk}^{(2)}(2w, w, w) E_j(w) E_k(w), \qquad 3.5$$

where indices ijk refer to the Cartesian components of the field. For the special case where the input laser field is horizontally polarized (x-direction), Eq. (3.5) becomes

$$P_i(2w) = c_{ixx}^{(2)}(2w, w, w) E_x^2(w). \qquad 3.6$$

In second-harmonic generation, not only the energy, but also the momentum has to be conserved. To achieve the highest efficiency of second harmonic generation, the phase mismatch $\Delta\mathbf{k} = \mathbf{k}(2w) - 2\mathbf{k}(w)$ must be close to zero. Therefore, if a single high intensity laser beam is used for SHG, the outgoing second-harmonic (SH) beam follows the direction of the outgoing fundamental beam. After these beams are spatially separated, the SH beam is easily detectable.

Electric-Field Induced Second Harmonic Generation

Second-harmonic generation (SHG) and, more specifically, time-dependent electric field-induced second-harmonic (TD-EFISH) generation are contactless, non-destructive techniques for probing surface and interface dynamics in semiconductor heterosturctures. SHG is an effective and sensitive tool for monitoring carrier dynamics especially in systems with regions of broken inversion symmetry such as at surfaces and interfaces. The presence of a dc electric field also breaks the inversion symmetry and can greatly enhance SHG signals[23]. This phenomenon is called electric-field-induced second-harmonic (EFISH[24]) generation.

There are three possible sources for electric fields in the crystal. An electric field may be intrinsic to the system under study (E_{0i}). This is true at the interface between two different materials, such as at a semiconductor heterojunction, in which the different band energies of the two materials create a depletion region at the interface, which has an intrinsic electric field.[15] Intrinsic electric fields are time-independent. An electric field may be induced in the material by placing the material in an externally generated electric field, or by appling a bias across the material using contacts (E_{EXT}). This type of electric field is externally controlled by the investigator, and is particularly useful in probing the behavior of semiconductor device structures[25,26]. Finally, an electric field can be induced by generating free charges in the material and somehow causing charge separation ($E_i(t)$). This type of electric field is particularly useful in investigating the charge dynamics at interfaces and surfaces, since there is no external influence on the system other than that stimulating the charge generation.

The intensity of second harmonic generation, including the EFISH contribution is given by

$$I^{(2w)}(t) = \sum_i \left| c_i^{(2)} + c_i^{(3)} \left(\pm E_{0i} \pm E_{EXT} \pm E_i(t) \right) \right|^2 \left(I_i^{(w)} \right)^2 \qquad 3.7$$

where $I_i^{(w)}$ and $I^{(2w)}$ are the intensities of the fundamental beam and the SHG signal, and $c_i^{(2)}$ and $c_i^{(3)}$ are the effective second and third order susceptibilities respectively. E_{0i} is the intrinsic electric field, E_{EXT} is an externally applied electric field, and $E_i(t)$ is the photo-induced electric field. The subscript "i" represents the contribution of each interface.[27]

SHG predominantly measures the electric fields at the interfaces of heterostructures. In this dissertation, SHG will be used to measure these interfacial electric fields of the GaSb/GaAs and InAs/GaSb/GaAs samples. In both samples, carriers are excited by the absorption of photons with photon energy above the bandgap of the semiconductor layers. The electrons and holes then have a tendency to accumulate in different layers causing interfacial electric fields, which is easily detectable using SHG.

CHAPTER IV

EXPERIMENT CONFIGURATION

Ti:Sapphire Laser

The workhorse for ultrafast studies in all branches of science during the 1980's was the Colliding pulse mode (CPM) dye laser[28]. However, these lasers were difficult to operate and maintain. Alternatively, a series of broad-bandwidth solid-state laser materials were developed, with the most notable of these being the titanium doped sapphire (Ti:Al_2O_3) laser, which lased over a continuous band stretching from 680 nm to 1100 nm. In late 1989, a group at MIT reported 200 fs pulses generated from a Ti:sapphire laser[29]. They used a novel mode-locking technique called *additive pulse mode-locking* (APM). The APM is accomplished by feeding back into the laser part of its output after it has been nonlinearly modulated in an external cavity. In 1991 a very exciting result was reported by Spence *et al*.[30] at the University of St. Andrews. They observed *self-modelocking* or *Kerr lens mode-locking* (KLM) of a Ti:sapphire laser. This type of mode-locking is induced in a solid-state laser because of the nonlinearity present in the laser crystal. The nonlinear index of refraction n_{nl} introduces an intensity dependent index given by

$$n = n_0 + n_{nl} I, \qquad 4.1$$

where n_0 is the linear index of the crystal, and I is the instantaneous laser pulse intensity. The nonlinear phase delay of the beam will be highest at the center of the beam when it focuses into the crystal, causing self-focusing. Therefore, there is an additional lens in the cavity with an intense pulse, which is not there for low-intensity light. The cavity alignment can be adjusted so that the pulse spatial mode suffers less loss than the CW spatial mode. When self-focusing is induced the mode-locked profile will match the pump mode, and will favor pulse operation. Because this mode-locking is induced by the pulse itself, the laser is said to self-mode-locked, and the effect is the same as if a fast saturable absorber were present in the cavity. Today Ti:sapphire lasers can generate 25 fs pulses without much difficulty, allowing researchers to explore semiconductor dynamics at very short time scales. Jung and co-workers[31] have demonstrated 6.5 fs pulses from a Ti:sapphire laser using a combination of a prism pair and a double chirped mirror for dispersion compensation. This development makes the modelocked Ti:sapphire laser ideal for extreme ultra-fast studies in semiconductors.

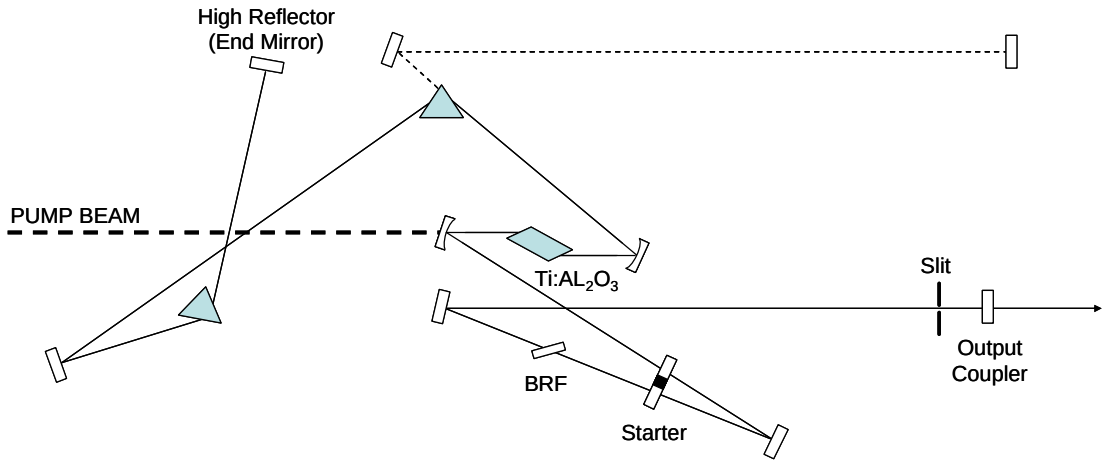

Figure 4.1. A schematic diagram of a typical self mode-locked Ti:sapphire laser.

The laser that is used in these experiments is The Coherent Mira 900, with the laser schematic shown in Figure 4.1.[32] It is a modelocked ultra-fast Titanium:sapphire laser that is tunable from 720nm to 900nm. The technique used to modelock the Mira laser is Kerr Lens Modelocking (KLM) that has been described above. The optical cavity is specifically designed to utilize changes in the spatial profile of the beam produced by self-focusing from the optical Kerr effect in the Titanium:sapphire crystal. This self-focusing results in higher round trip gain in the modelocked (high peak power) versus CW (low peak power) operation due to an increased overlap between the pumped gain profile and the circulating cavity mode. Also, an aperture is placed at a position within the cavity to produce lower trip loss in the modelocked versus CW operation. The Brewsters prisms (shown in Figure 4.1) are used for group velocity dispersion compensation.

Pump-Probe Technique

Pump-probe measurements can be used to obtain information on an ultra-fast time scale. A schematic diagram of a typical setup for time-resolved reflection experiment[2] is shown in Figure 4.2. An ultra-fast laser pulse is divided into two pulses using a beam splitter: the pump and the probe. The pump is the more intense of the two. The probe pulse is much weaker in order to produce the minimum perturbation on the sample. The ratio of pump to probe intensities is typically at least 10:1. The separated beams follow different optical paths with the probe having a variable path length. Varying the path length will in effect vary the time delay between the pump and probe pulses. The delay is typically done with a precise motorized transitional stage due to the extreme accurate

requirements for temporal resolution. Following the different optical paths the pump and probe beams are then directed and focused on the same spatial area on the sample. Typically the pump spot size is always slightly larger than the probe spot size. This is to ensure that the probe beam is completely within the excitation beam. The pump pulse excites and modifies the optical properties of the sample and the probe pulse monitors this change as a function of the optical time delay between the two pulses. The reflection (transmission) beam is detected with a photodiode.

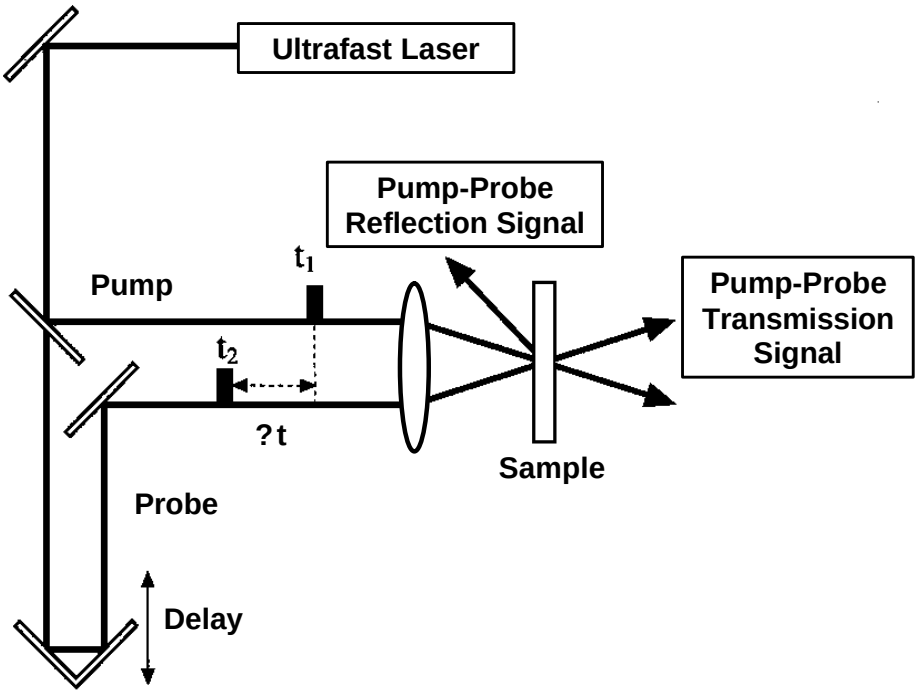

Figure 4.2. Schematic diagram of a generic setup for a pump-probe experiment. This setup can be used for pump-probe reflection or transmission spectroscopy. The ultrafast laser pulse is separated into a pump and a probe beam with a variable optical delay between them (?t). The pump beam is used to excite the semiconductor, whereas the probe beam (usually much weaker than the pump beam) is used to measure the changes induced by the pump pulse as a function of the optical delay between them.

Experiment Setup

The specific pump-probe setup that was used for this body of work is shown in Figure 4.3. In this setup, a Newport translation stage is used for the delay line and a time delay of approximately 1000 ps can be observed. To improve the sensitivity of the experiment a lock-in amplifier is utilized along with an acousto-optic modulator (AOM) (see Appendix D). The AOM is placed in the path of the pump beam, which modulates the excitation, thus giving a synchronization signal to the lock-in amplifier.

One unique capability of this experimental setup is that there are two separate channels that can measure two different signals simultaneously. One channel measures the pump induced second harmonic generation signal and the other channel measures the

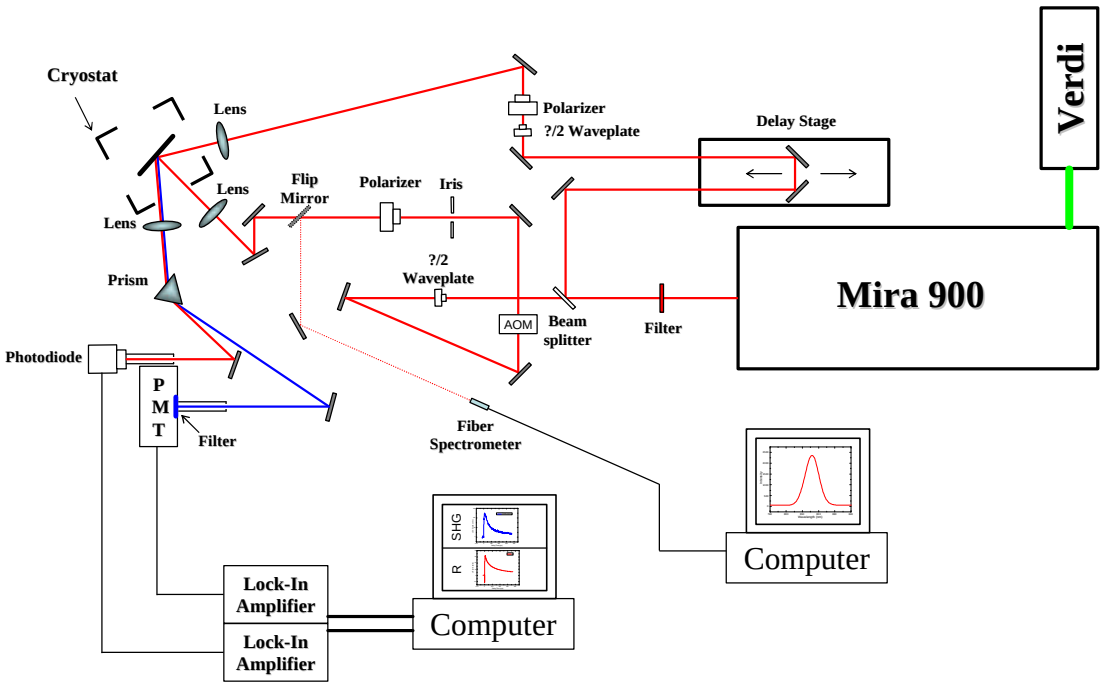

Figure 4.3. The specific pump-probe setup that is used at Vanderbilt University.

differential reflectivity. The two signals are spatially separated using a prism. The SHG signal is measured with a Hamamatsu Type R4632 photomultiplier tube (PMT) and the fundamental reflection signal is measured with a ThorLabs DET210 photodiode.

CHAPTER V

ULTRA-FAST CARRIER AND PHONON DYNAMICS

Introduction

Many experiments using pump-and-probe techniques to investigate the temporal behavior of semiconductors have been performed. Most of these experiments have separately probed various aspects of nonequilibrium carrier and phonon dynamics on a picosecond or subpicosecond time scale. Although much of the effort has been placed on understanding nonequilibrium carrier kinetics alone, nonequilibrium phonons can influence hot carrier relaxation and transport.[33,34]

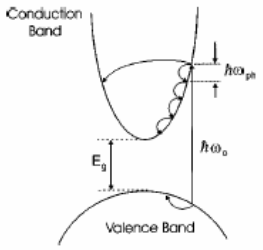

Figure 5.1. A schematic illustration of the electron-hole pair excitation using laser radiation of energy $\hbar w_0$. Energy relaxation follows via optical phonon emission ($\hbar w_{ph}$).[35]

Energy Relaxation in Semiconductors

Illumination of a semiconductor with photons that have above band gap energy results in the generation of excess (nonequilibrium) carrier densities and elevated carrier temperatures.[36] Depending on the incident fluence and the photon energy of the laser radiation, particle densities several orders of magnitude above the equilibrium value may be reached and carrier temperatures of several thousand degrees may be obtained. This in turn will affect various macroscopic parameters such as those governing the optical properties of the system.

Part of the radiation incident on a semiconductor is reflected and part of it enters the solid where some of it is absorbed and the rest transmitted.[37] Linear absorption occurs when the photon energy is larger than the bandgap of the semiconductor[38,39] (Figure 5.1). In direct optical absorption a quantum of light from the laser pulse is absorbed by an electron, thus making a transition from the valence to the conduction band. This produces a hole in the valence band.

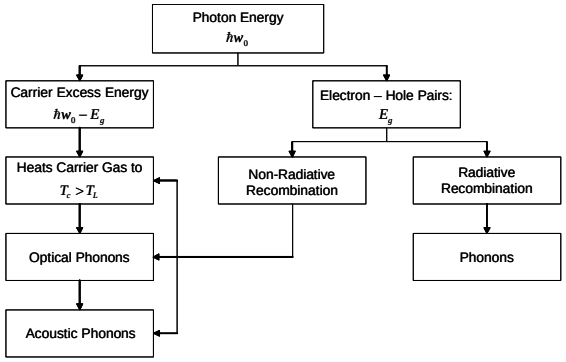

Figure 5.2. A block diagram illustrating the flow of energy in photoexcited semiconductors. This diagram shows the evolution of laser deposited energy in the carrier and lattice systems, where only single-photon interband absorption is considered.[40]

After electrons and holes are optical excited, they undergo spatial and temporal evolution with characteristic times which depend on the various relaxation processes (see Table 5.1 and Fig. 5.2).[40] Initially, the excitation energy is transferred entirely to the carriers, leading to the creation of nonequilibrium carrier densities with specific momentum states and elevated carrier temperatures. As the system evolves towards equilibrium there is momentum and energy relaxation. Momentum relaxation occurs on a femtosecond time scale via elastic and inelastic scattering. Carrier–carrier scattering of the electrons (holes) results in carrier thermalization and allows the electron (hole) system to be described by a Fermi–Dirac distribution with temperature T_e (T_h). This occurs on a femtosecond time scale. Similarly, electron-hole scattering eventually brings the two distributions into thermal equilibrium.

Energy relaxation of carriers occurs primarily via the emission of optical phonons.[41] For the holes this interaction involves optical phonons generated near the center of the Brillouin zone. However, in addition to small wave-vector phonon emission,

Table 5. 1. Fundamental processes in semiconductors.[40]

Microscopic Process	Characteristic time(s)
Carrier-carrier scattering	10^{-15}-10^{-12}
Intervalley scattering	$=10^{-14}$
Intravalley scattering	$\sim 10^{-13}$
Carrier-optical phonon thermalization	$= 10^{-12}$
Optical phonon-acoustic phonon interaction	$\sim 10^{-11}$
Carrier diffusion (0.1um)	$\sim 10^{-11}$
Auger Recombination (carrier density 10^{20} cm^{-3})	$\sim 10^{-10}$
Radiative recombination	$= 10^{-9}$
Lattice heat diffusion (1μm)	$\sim 10^{-8}$

conduction band electrons can interact with large wave-vector phonons. This involves the scattering of electrons from the central valley of the Brillouin zone to the various side valleys (intervalley scattering) resulting in large wave-vector phonon emission.[42,43] All optical phonons generated eventually decay into two or more lower energy phonons (LA+LA or LA+LO, etc.) via multiphonon processes associated with lattice anharmonicity (Fig. 5.3). This decay time depends on the lattice temperature, which for the zone center optical phonons varies from ~10 ps at cryogenic temperatures to ~4 ps or less at room temperature.[44] Because this time can be longer than the carrier–optical phonon thermalization time, large nonequilibrium optical phonon populations can occur during carrier energy relaxation. These ‘‘hot phonons’’ can inhibit energy relaxation of the carriers (hot phonon re-absorption).[33,34]

On a time scale greater than 100 ps (depending on the carrier density) electron–hole recombination occurs at high carrier densities via the three-body Auger process. Other recombination processes take place on even longer time scales and therefore are considered negligible for the ultra-fast time domain.

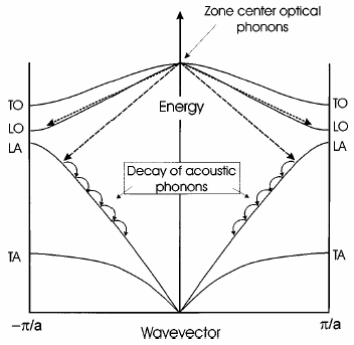

Figure 5.3. A schematic illustration of relaxation processes of optical and acoustic phonons in germanium. The zone center phonons decay into different phonon modes under the restriction of conservation of energy and momentum.

Ultra-fast Laser Pulse Excitation

Under equilibrium conditions in semiconductors, free electrons and holes behave according to Fermi-Dirac statistics, whereas phonons follow Bose-Einstein statistics. In the absence of an external force, energy and momentum interchange through carrier-carrier and carrier-phonon interactions that keep the three distributions (electrons, holes, and phonons) at a common temperature. The average momentum of the carrier and

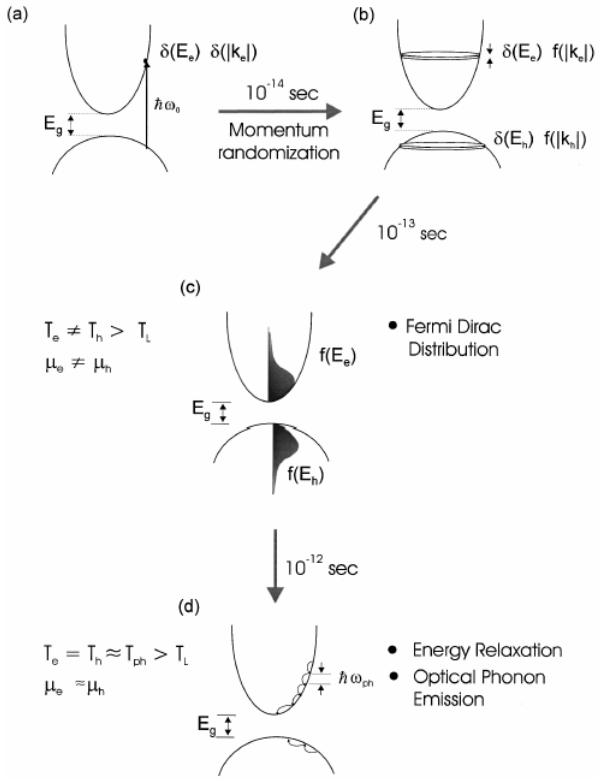

Figure 5.4. A schematic diagram illustrating the photo-excitation of a semiconductor and subsequent energy relaxation. (a) Initially after photo-excitation with polarized light, the carriers will have delta function distribution in momentum and energy space. (b) Within tens of femtoseconds momentum randomization occurs. (c) Thermalization of carriers into a Fermi-Dirac distribution for carrier densities greater than 10^{19} cm^{-3} via collision occurs on 10^{-13} s. (d) As time evolves the hot carriers lose their excess kinetic energy while attempting to reach thermal equilibrium with the lattice through optical phonon scattering.[35]

phonon systems under this condition is zero, with their average energies corresponding to their common temperature. When an external force is applied (example: absorption of electromagnetic radiation) the equilibrium of the semiconductor is disturbed and under such a condition the two systems may have different thermal states. As soon as the external force is removed, the carriers return to equilibrium.

The average momentum relaxes back to zero, while the average carrier temperature relaxes to the lattice temperature value as carriers lose momentum and energy to phonons through various scattering processes. The relaxation rate of the momentum and energy of the carriers to the equilibrium value is determined by the nature of the scattering, and the number of the processes involved.

The major processes that follow the photo-excitation of a semiconductor with an ultra-fast pulse are shown in Figure 5.4.[35] Absorption of an ultrafast pulse by a semiconductor where the photon energy $\hbar w_0$ is larger than the bandgap energy E_g results in the creation of electron-hole pairs with excess kinetic energy that corresponds to the residual energy $\hbar w_0 - E_g$. This initial excitation by an ultrafast pulse produces distributions of electrons and holes that are narrow in energy and peaked in a particular direction of momentum space [Fig. 5.4(a)]. However, elastic as well as inelastic scattering events randomize the momentum within tens of femtoseconds (Fig.5.4(a)-5.4(b)).

After excitation the electrons will retain most of the excess kinetic energy since their effective mass is much lighter than that of holes. Therefore, electrons and holes have to be considered as separate systems each with their individual thermal distributions. Electron-electron and hole-hole collisions are density dependent. For

carrier densities greater than 10^{19} cm^{-3} these collisions occur on 10^{-13} s time scale which thermalizes the carriers into a Fermi-Dirac distribution (Fig.5.4(b)-5.4(c)). The distribution functions for electrons and holes possess different temperatures which may be higher than the lattice temperature depending on $\hbar w_0$. As time evolves the hot carriers lose their excess kinetic energy while attempting to reach thermal equilibrium with the lattice through various scattering mechanisms, with the most efficient mechanism being the optical phonon scattering.[2] Through interaction with the carriers, the population of the nonequilibrium optical phonons increases and, on a picosecond time scale, attempts to thermalize with other lattice modes through phonon-phonon interactions.

Strain Generation

In general, consider when an energetic pump pulse is incident upon the surface of a sample. The light pulse changes the electron and phonon distribution functions $n_e(\mathrm{k})$ and $n_p(\mathrm{k})$ by $\mathrm{d}n_e(\mathrm{k})$ and $\mathrm{d}n_p(\mathrm{k})$, respectively. These changes produce a stress which is given by[45]

$$s_{ij} = \sum_k \mathrm{d}n_e(\mathrm{k}) \frac{\partial E_{\mathrm{k}}}{\partial n_{\mathrm{ij}}} + \sum_k \mathrm{d}n_p(\mathrm{k}) \hbar \frac{\partial w_{\mathrm{k}}}{\partial n_{\mathrm{ij}}}, \qquad 5.1$$

where E_{k} and w_{k} are the energy of an electron and the frequency of a phonon of wave vector k, respectively. The first term in Eq. (5.1) is an electronic contribution to the

strain associated with the deformation potential $\frac{\partial E_{\mathrm{k}}}{\partial n_{\mathrm{ij}}}$. If the electrons and phonons are in local thermal equilibrium then Eq. (5.1) reduces to[45]

$$-3Bb\Delta T(z), \qquad 5.2$$

where B is the bulk modulus and b is the linear expansion coefficient.

In semiconductors, the absorbed pump photons will excite electrons and holes which emit phonons and relax to the band edge in a short time (~ 1 psec). Recombination occurs on a much longer time scale (= 1 nanosecond).[40] From Eq. (5.1) the electron-hole contribution to the stress is

$$s_{ij}^{e} = \frac{\partial E_g}{\partial n_{ij}} dn_e = -B\frac{dE_g}{dP} d_{ij} dn_e, \qquad 5.3$$

where dn_e is the total number of electrons (equal to the total number of holes), E_g is the bandgap, P is the pressure, and the assumption has been made that the solid is elastically isotropic. For each photon of energy E which is absorbed, thermal phonons of total energy $\left(E - E_g\right)$ are produced. If these phonons are well described by a thermal distribution, their contribution to the stress is[46]

$$s_{ij}^{p} = -\frac{3Bb}{C}(E - E_g)d_{ij}dn_e. \qquad 5.4$$

The electrons and phonons reach thermal equilibrium so that both can be described by a single temperature and their contributions to the strain can not be distinguished. This process takes on the order of a few picoseconds.[40] The experimental data shown in Chapter VII reveals that the oscillations due to coherent phonons typically do not start until after a delay time of at least 10 picoseconds. Therefore, our electron-phonon system has reached thermal equilibrium and can be regarded as a single contribution to the strain (Eq. 5.2).

Strain Detection

A probe pulse is used to detect the propagation of the strain pulse as shown in Figure 5.5. It has a time delay ? t relative to the generating pump pulse. The measured signal is the result of interference between the probe beams reflected from the air/bulk interface and the bulk/strained layer boundary These two reflected beams interfere constructively or destructively depending on the distance $z(t)=V_s t$ traveled by the strain pulse. Therefore, the total reflected intensity will be oscillatory in time.

The oscillation period T can be calculated to be

$$T = \frac{l}{2nV_S \cos q}, \qquad 5.5$$

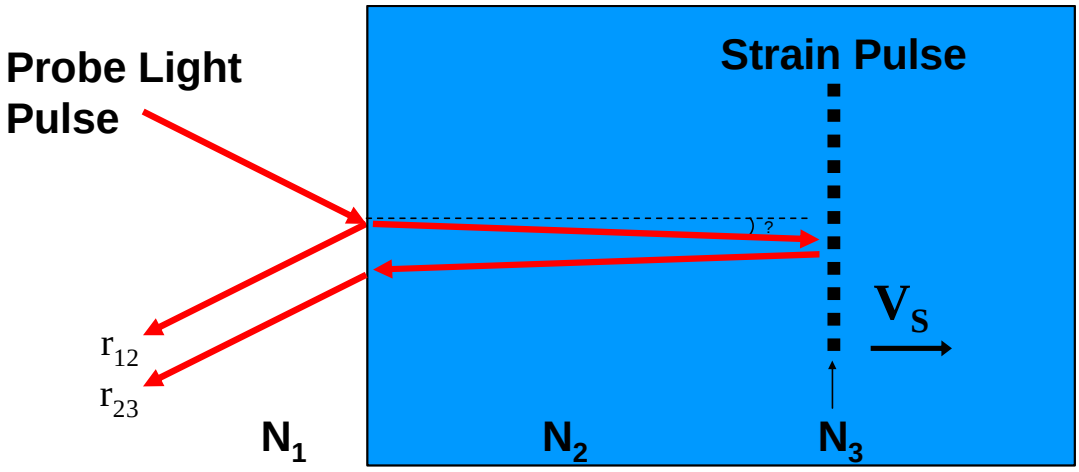

Figure 5.5. A schematic diagram of the experiment.

where l is the probe wavelength, n is the index of refraction of the material, V_S is the speed of LA phonons, and q is the incident angle of the probe light in the bulk semiconductor.

The reflection coefficient in this three layer system[47] is

$$R = \left| \frac{r_{12} + r_{23} e^{2ikz}}{1 + r_{12} r_{23} e^{2ikz}} \right|^2 , \qquad 5.6$$

where $r_{ij}=(N_i-N_j)/N_i+N_j)$ is the Fresnel reflection amplitude from the boundary between media i and j, and N_i is the complex index of refraction of media i. Here N_1=1 in air, $N_2=N(\omega)=n(\omega)+ik(\omega)$ in the bulk semiconductor, $N_3=N(\omega)+\delta N(\omega)$ in the strained layer, and $k=(\omega/c)N\cos\theta$ is the normal component of the wavevector in the bulk semiconductor. Thus we define r_{12} as the reflection amplitude from the air/GaSb boundary, and r_{23} ~

dN/N describes reflection from the moving strained layer. Since the strain-induced change in refraction index, *dN*, is small, a simple expression for R can be obtained by expanding Eq. (5.6) in the first order in small parameter the reflection coefficient r_{23}. If we assume $r_{ij} = \rho_{ij} e^{i\phi_{ij}}$ (where ρ_{ij} is the amplitude and ϕ_{ij} is the phase of the reflection amplitude r_{ij}), then the differential reflection

$$\frac{\Delta R}{R_0} = \frac{(R - R_0)}{R_0}, \qquad 5.7$$

with $R_0 = |r_{12}|^2$, takes the form[48]

$$\frac{\Delta \mathbf{R}}{\mathbf{R}_0} \approx 2|r_{12}||r_{23}|\sqrt{1+\rho_{12}^4+2\rho_{12}^2\cos(2\phi_{12})}\,e^{-\frac{t}{\tau}}\sin\left(\frac{2\pi}{T}t+(\varphi_0+\varphi_{12}+\varphi_{23})\right) = Ae^{-\frac{t}{\tau}}\sin\left(\frac{2\pi}{T}t+\varphi_{init}\right) \qquad 5.8$$

where $A \propto \frac{\delta N}{N}$ is the amplitude, *T* is the period, and j_{init} is the initial phase, which includes phase shifts j_0, j_{12}, and j_{23} from the GaSb layer, reflection coefficients r_{12} and r_{23}, respectively. The phase shifts j_{12} and j_{23} are given by

$$\varphi_{12} = \sin^{-1}\left(\frac{\left(1+|r_{12}|^2\right)\cos(\phi_{12})}{\sqrt{\left(1+|r_{12}|^4\right)+2|r_{12}|^2\cos(2\phi_{12})}}\right) \qquad 5.9$$

and

$$j_{23} = \arg(r_{23}). \qquad 5.10$$

The period T is given by Eq. (5.5) and the damping time is defined as,

$$t = \frac{l}{4pkV_S \cos q} = \frac{Tn}{2pk}, \qquad 5.11$$

where k is the imaginary part of the complex index of refraction of the bulk semiconductor and is related to the absorption coefficient a by

$$a = \frac{2wk}{c}. \qquad 5.12$$

The penetration depth, z , is the reciprocal of the absorption coefficient ($z = a^{-1}$). The amplitude of oscillations depends linearly on the strain-induced change in the refraction coefficient. The latter is determined by local reduction of the bandgap δE_g due to the lattice expansion in the strained layer. The oscillation amplitude, $A \propto \delta N/N$, is then related to δE_g as

$$A \propto \left| \frac{\partial N}{\partial w} d E_g \right|, \qquad 5.\ 13$$

where the magnitude of δE_g depends both on the intensity and frequency of pump beam. A more detailed model can be found in Ref [46], which also leads to Eq. (5.8).

CHAPTER VI

ULTRA-FAST CARRIER DYNAMICS USING SECOND HARMONIC GENERATION

Measurements of the ultrafast dynamics of optically induced interfacial electric fields in semiconductor multilayers using SHG as a probe were conducted using the setup in Figure 4.3. The advantage of this technique is the ability to simultaneously monitor the carrier dynamics at different interfaces of the same sample. In particular, by tracking the evoultion of different interfacial fields contributing to the total electric-field-induced second harmonic (EFISH) generation signal we are able to study the redistribution of carriers between the layers due to electron transport across interfaces.

These measurements were preformed on GaAs/GaSb and GaAs/GaSb/InAs heterostructures and the results are shown in Figure 6.1. The pump-induced SHG signal for the GaAs/GaSb heterostructure is described by a single rise-time constant, $t_R \sim 1$ ps, and a single decay time constant, $t_D \sim 150$ ps. The pump-induced SHG signal for the GaAs/GaSb/InAs heterostructure is described by two rise-time constants, $t_{R_1} \sim 1$ ps and $t_{R_2} \sim 10$ ps, and a single decay time constant, $t_D \sim 150$ ps.

An apparent presence of several stages in the evoultion of the measured SHG signal indicates the rather complicated dynamics of interfacial electric fields originating from a redistribution of carriers between the interfaces. The induced local electric fields, $E_1(t)$ and $E_2(t)$ (subscripts 1 and 2 refer to the GaAs/GaSb and GaSb/InAs interfaces, respectively), depend on the number of carriers near each interface at a given time.

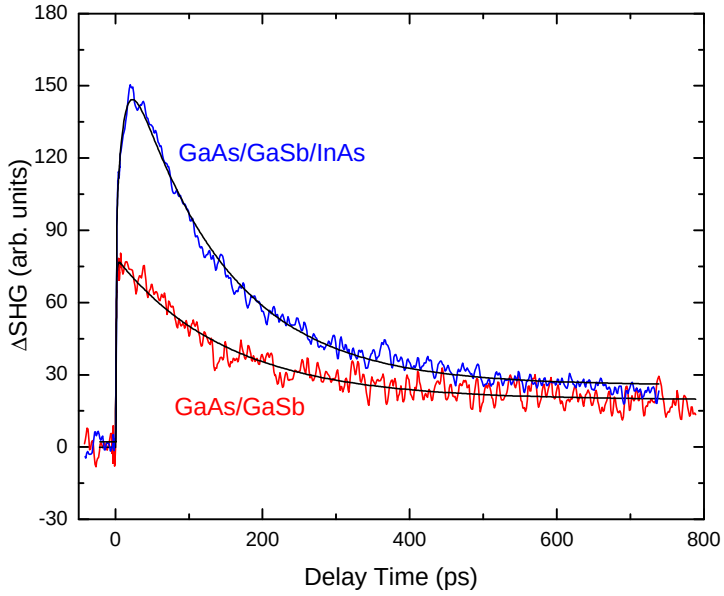

Figure 6.1. Experimental ? SHG data for GaAs/GaSb (red) and GaAs/GaSb/InAs (blue) samples. The measured signals were fitted by a combined exponential rise and decay function (black).

We attribute the observed several stages in the dynamics of the interfacial electric fields to an interplay between relaxation of carriers and their transport across the heterostructures. Since carriers are excited in all the heterostructure layers, electrons with high excess energies relax to the lower energy conduction band states in the GaAs and InAs layers, while the holes are accumulated in the GaSb layer (Figure 6.2). The resulting charge seperation leads to a rise of the interfacial fields which manifests itself in the initial growth of the EFISH signal characterized by the fast rise-time constant (~ 1 ps) in both samples. The induced interfacial fields bend the initial energy profile, thus lowering the barrier at the GaAs/GaSb interface (Fig. 6.2) and resulting in electron transport across the interface.

For the GaAs/GaSb/InAs heterostructure we see this additional rise in the SHG signal. In this case, the electrons crossing the GaAs/GaSb interface accumulate in the InAs layer. The resulting increase in the GaSb/InAs interfacial field manifests itself as the additional rise component of the EFISH signal with the rise-time constant $t_{R_2} \sim 10$ ps. The subsequent relaxation of the interfacial electric fields is characterized by $t_D \sim 150$ ps decay time constant.

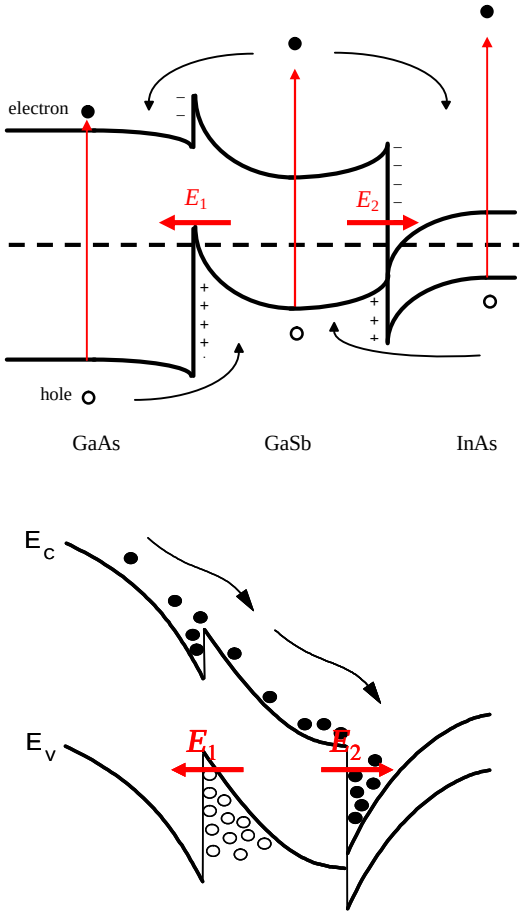

Figure 6.2. The initial band alignment for GaAs/GaSb/InAs heterostructure (a) and its realignment due to induced electric fields (b).

Using SHG, the ultrafast dynamics of the interfacial electric fields in different heterostructures can be studied. In this case, a complicated evolution of the interfacial electric fields originating from the redistribution of carriers between the interfaces can be observed. The ability of the EFISH signal to monitor spatially separated regions makes pump-probe SHG a unique tool for studying relaxation and transport phenomena in multilayer semiconductor structures.

CHAPER VII

NEAR-BANDGAP WAVELENGTH-DEPENDENT STUDIES OF LONG-LIVED TRAVELING COHERENT LONGITUDINAL ACOUSTIC PHONON OSCILLATIONS

Coherent phonon oscillations generated by ultrafast optical excitation has been observed in various material systems using time resolved pump-probe schemes[46,49,50,51,52]. In these experiments, femtosecond pump light pulses are absorbed at sample surfaces, resulting in the generation of coherent phonons. The time delayed probe pulses sense the coherent phonon modulation of optical properties, such as reflectance or transmittance. In particular, traveling coherent longitudinal acoustic phonon (CLAP) waves have been recently reported in a wide range of materials, including manganites[53], and III-V semiconductors[54,55,56]. Here, the photo-induced acoustic phonon wave generated near the surface travels into the substrate following excitation. The oscillations in the pump-probe reflectance responses arise from interference between probe light reflected from the front surface and from the traveling coherent longitudinal *acoustic* phonon plane wave. This is in contrast to the observed short-lived, fast oscillations arising from the coherent *optical* phonon modulation of the optical properties of the near surface.

CLAP Waves Produced in GaAs/GaSb Systems

We report here first observations of long-lived traveling coherent longitudinal acoustic phonon (CLAP) waves in the GaSb/GaAs system. The oscillatory response is strongly dependent on the probe light wavelength near the band gap of GaAs and persists

for the entire measuring time window and beyond. Since the traveling CLAP wave differentially samples the material as it proceeds from material to material across interfaces, it constitutes a promising non-invasive technique for measuring optical properties of the material as a function of depth. It is also a useful tool for measuring layer thicknesses and band gap energies.

We investigated GaSb/GaAs heterostructures, grown by standard molecular beam epitaxy (MBE) using a Riber 32 R&D MBE machine at the University of Notre Dame. First, a semi-insulating "epi-ready" (001) GaAs substrate is heated to 600^{o}C under As_2 flux for deoxidization. After this thermal cleaning, a 100nm GaAs buffer layer is grown on substrates at normal GaAs growth conditions (~600^{o}C) in order to obtain an atomically flat surface. Finally, a layer of GaSb is grown at 490^{o}C.

Standard femtosecond, time-resolved optical pump-probe measurements of transient reflectivity change $\Delta R/R$ are performed on these samples. The light source is a Coherent MIRA 900 Ti:Sapphire laser, which produced 150-fs-wide pulses in the 740 nm (1.675 eV) to 890 nm (1.393 eV) wavelength range at a repetition rate of 76 MHz. The oscillatory response can be observed at all temperatures from 4 K up to room temperature, and we did not observe strong temperature dependence of the oscillatory signal. However, the bandgap of GaAs shifts with temperature. Here we choose 30 K for our systematic wavelength dependent study, since the bandgap of GaAs at 30 K (1.517 eV or 817 nm in optical wavelength) is in the middle of our Ti:Sapphire laser's wavelength tuning range, while the room temperature bandgap of GaAs is very close to the upper limit of the tuning range (1.424 eV or 870 nm). The pump and probe beams are cross-polarized and their spot sizes on the sample are about 100 *m*m in diameter, with

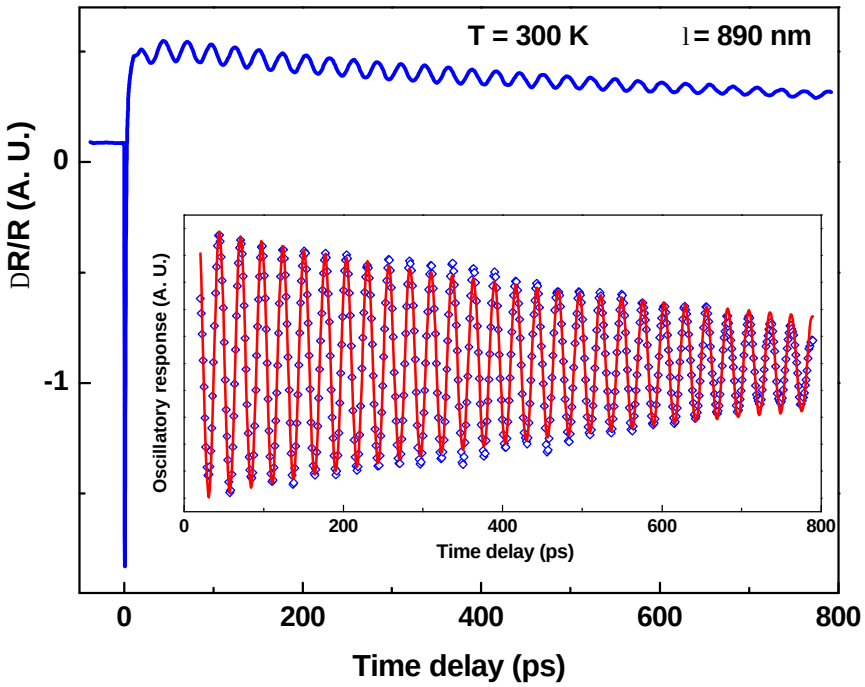

Figure 7.1. Total pump-probe response of GaSb(20 nm)/GaAs at 890 nm at 300 K. Inset: the subtracted oscillatory response (open diamond) fitted with a damped oscillation simulation (solid line).[48]

their energy ratio of 10:1. Typical pump light has an average power of 30 mW, equivalent to a pulse energy of 0.4 nJ and a fluence of 5.1 μJ/cm^2. This excitation intensity is about 3 orders of magnitude smaller than the intensity in some references, where an OPA system is typically used. The pump beam is incident normal on the sample while the probe is at an angle of 45°.

In Figure 7.1, we show the measured pump-probe response at room temperature on a sample with a relatively thin, 20 nm GaSb layer, on a GaAs substrate. The wavelength is 890 nm (1.393 eV), slightly below the bandgap of GaAs (1.424 eV) at room temperature, but above the bandgap of GaSb (0.8 eV). It is clear that the total

response consists of a fast transient (on the order of a few picoseconds) followed by a very long-lasting damped oscillatory tail. The initial fast transient is typical for carrier dynamics due to the excitation of hot photoexcited electron-hole pairs and relaxation by means of electron-phonon interaction in GaSb. The long-lasting oscillations are not directly related to the pump light since it only appeared after the first fast transient. The inset is the measured oscillatory response (open diamond), which is obtained by subtracting the thermal relaxation background, fitted with an exponentially damped oscillation function (solid line). Applying the fitting curve to the data, we obtain a period of oscillation of about 26.6 ps and the damping time of about 720 ps.

The origin of this class of oscillations was explained first by Thomsen *et al.* in 1986.[46] Namely the ultra-fast pump pulse is absorbed at the surface of the film and the absorbed photon energy gives rise to a transient electron and phonon temperature increase within the illuminated area, which then sets up a transient stress at the sample surface. This stress induces a strain wave (coherent longitudinal acoustic phonons), which propagates away from the surface at the speed of the LA phonons. This CLAP wave modifies the local dielectric constants and creates a discontinuity. When the probe pulse is incident onto the sample, part of the light is reflected from the top surface of the sample, and the rest of the transmitted light reaches the CLAP wave inside and gets partially reflected due to the discontinuity in the dielectric constants. As the CLAP wave travels, the top surface and the strain wave surface act as a 'Fabry-Perot' interferometer. Oscillations arise from the fact that the distance between the two surfaces is constantly changing, causing a periodic phase difference between the two reflected beams.[57]

In the GaSb/GaAs system, the top layer of GaSb is an absorber to create the phonon wave after photon excitation. The bandgap of GaSb is 0.8 eV, much smaller than the pump photon energy within the whole wavelength tuning range. On the other hand, the GaAs substrate has a bandgap very close to the pump photon energy. The absorption coefficient is about 5 times bigger in GaSb compared to GaAs at 1.5 eV[58]. Thus we assume that the pump photon energy is absorbed in the GaSb layer only. A temperature increase in GaSb due to excitation happens after the initial excitation of electrons and holes and electron-phonon interaction. These processes take place in several picoseconds. From the model proposed by Thomsen *et al.*, it is clear that the wavelength of the pump light plays little role in creating phonon waves, as long as the excitation photon energy can be absorbed by the top layer of GaSb. The thickness of the GaSb layer is small (20 nm), so that we assume the whole GaSb layer is excited to generate the CLAP wave. The CLAP wave travels along the normal direction at the speed of the LA phonons. When the probe pulse reaches the sample after excitation, part of the light is reflected from the air/GaSb layer, and part of the light penetrates into the GaSb and eventually into the GaAs. The probe light is then reflected back from the CLAP wave and produces interference with the reflected light from the air/GaSb surface with a given oscillation period T given by Eq. (5.5). For the probe wavelength of 890 nm, as shown in Figure 7.1, we use values from the literature: $n = 3.65$[58], $V_s = 4.73 \times 10^3$ m/s[59] and an incident angle of 45 degrees of the probe light in the air. Using Eq. (5.5), the calculated period is 26.3 ps, in close agreement with the measured period of 26.6 ps.

We then perform wavelength dependent studies of the oscillations near the bandgap of GaAs and the oscillation data are illustrated in Figure 7.2. In both Fig. 7.1

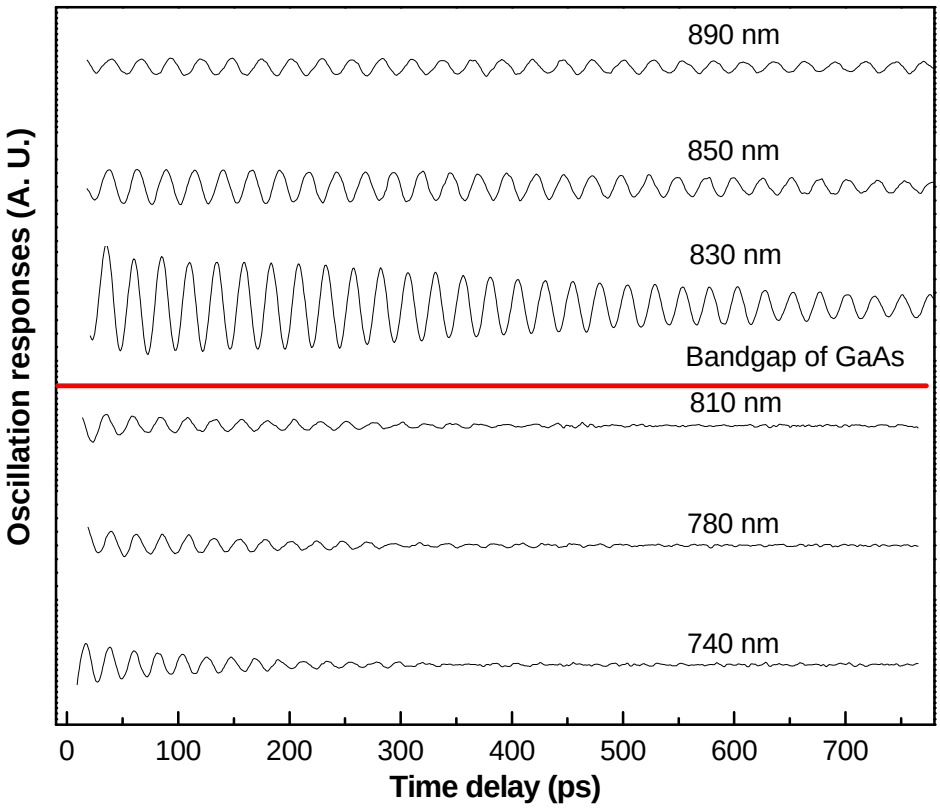

Figure 7.2. Oscillatory responses measured at different wavelengths at 30 K.[48]

and Fig. 7.2, the oscillations are seen to persist with little damping for at least 1 ns, for photon energies below the bandgap. Above the bandgap, this decay is not due to the decay of the phonon wave itself, but rather to the above-bandgap optical absorption of GaAs. Thus, we conclude that the CLAP wave, which does not depend on the probe wavelength, remains coherent without significant decay for at least 1 ns for all probe wavelengths. This is also in good agreement with the 'near-field' assumption in Ref. [46]. Similar long-lasting CLAP oscillations have been previously observed[51,55].

The model that was developed in Chapter 5 can be used to explain the experimental data shown in Fig. 7.2. The photoexcited carriers in the GaSb layer transfer their excess energy, deposited by the pump pulse, to LA phonons thus causing rapid expansion of the lattice on subpicosecond timescale. The propagating CLAP wave can be viewed as a strained layer moving away from the surface with LA phonon velocity Vs.

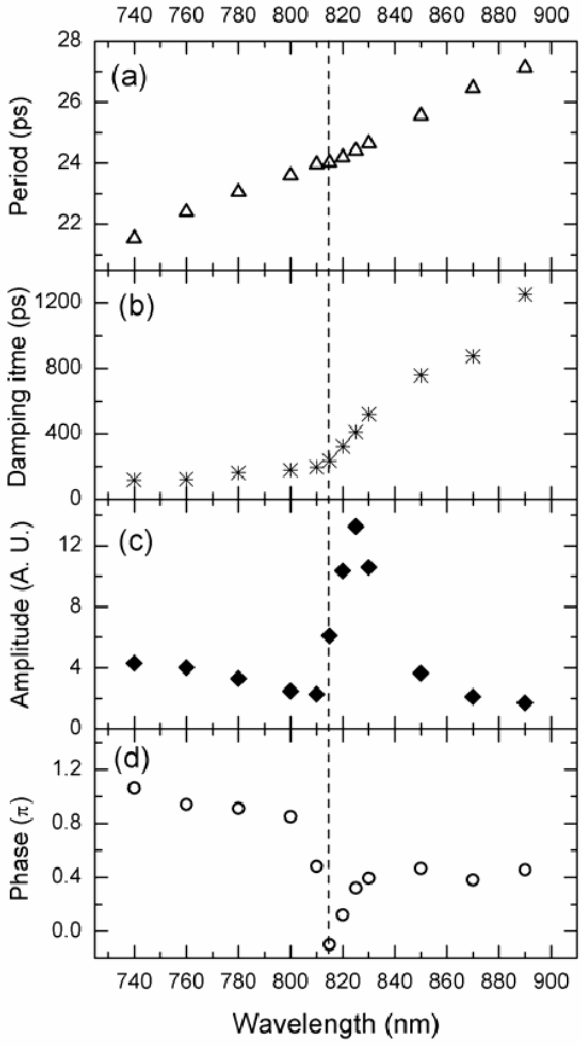

Figure 7.3. Wavelength dependence of the oscillations parameters fitted with Eq. 3 at 30 K. The dash-dot line indicates the bandgap of GaAs at 30 K. (a) Oscillation period (open triangle) (b) Damping time (star) (c) Amplitude (solid diamond) (d) Initial phase (Open circle).[48]

The measured signal is the result of interference between the probe beams reflected from the air/bulk interface and the bulk/strained layer boundary at the distance $z(t)=V_s t$ from the surface.

Figure 7.3 shows the period T, the damping time τ, and the amplitude A, and the initial phase j_{init}, as a function of the wavelength as numerical fits to the measured oscillation data using Eq. (5.8). Figure 7.3 (a) shows that the oscillation period is close to linear with the probe light wavelength, as predicted by the theoretical model (Eq. (5.5)). Small variation from linearity may due to the fact that index of refraction of GaAs is not constant at different wavelengths near the bandgap. This linearity of the oscillation period is a strong indication that a CLAP wave is indeed the origin of the long-lasting oscillatory response we observed. Figure 7.3 (b) shows the damping time τ at different wavelengths. As discussed, the damping time of the oscillations reflects the optical absorption of GaAs, or the imaginary part of the refractive index k (from Eq. 5.11). The onset wavelength of the increased damping time thus corresponds to the bandgap value from Fig. 7.3 (b), suggesting a new way to determine the bandgap of GaAs. This figure also suggests that the traveling strain wave remains coherent for at least 1 ns, which corresponds to a traveling distance of about 5 μm. We expect the damping time in GaAs to be even longer with longer probe wavelengths. Figure 7.3 (c) gives amplitude dependence. The amplitude of oscillations depends linearly on the strain-induced change in the refraction coefficient. The latter is determined by local reduction of the bandgap δE_g due to the lattice expansion in the strained layer. The oscillation amplitude, $A \propto \delta N/N$, is then related to δE_g as by Eq. (5.13), where the magnitude of δE_g depends

both on the intensity and frequency of pump beam. With increasing photon frequency, carriers with higher excess energy (with respect to GaSb bandgap) are created, leading to a larger energy transfer to the lattice. When the frequency is tuned away from the GaAs bandgap, this mechanism chiefly determines the oscillation amplitude. However, in the vicinity of the bandgap, $\omega \approx E_g$, the dielectric function of GaAs experiences a rapid change as the frequency passes through the absorption onset. Consequently, the derivative of N in Eq. (5.13) exhibits a sharp peak near the bandgap, resulting in a strong peak in the amplitude A in Fig. 7.3(c)). Figure 7.3 (d) shows the initial phase j_{init} in Eq. (5.8) at different wavelengths. The phase j_0 represents the phase difference between the two reflected light beams when the strain wave first enters GaAs, which is proportional to the GaSb thickness and inverse proportional to the probe wavelength.[51] Near the bandgap however, the phase j_{23} experiences a jump as indicated by the sharp dip in the figure. This phase discontinuity is caused by the anomalous behavior of the phase shift at reflection from the strained layer that is determined by the Fresnel reflection amplitude r_{23} in Eq. (5.8).

All the above measurements and analysis have been carried out on a GaSb/GaAs sample with a 20 nm GaSb top layer. We have neglected the possibility of oscillations due to the CLAP wave traveling inside the GaSb layer because of the relatively small thickness. When the GaSb layer becomes thicker, the CLAP wave can produce oscillations while still in GaSb as well. Oscillations due to the CLAP wave in GaSb have been reported recently[54]. Our focus here is to observe how the pump induced CLAP wave propagates through two different materials, in our case GaSb and GaAs, which has not been studied previously. Figure 7.4 shows the measured oscillatory responses of

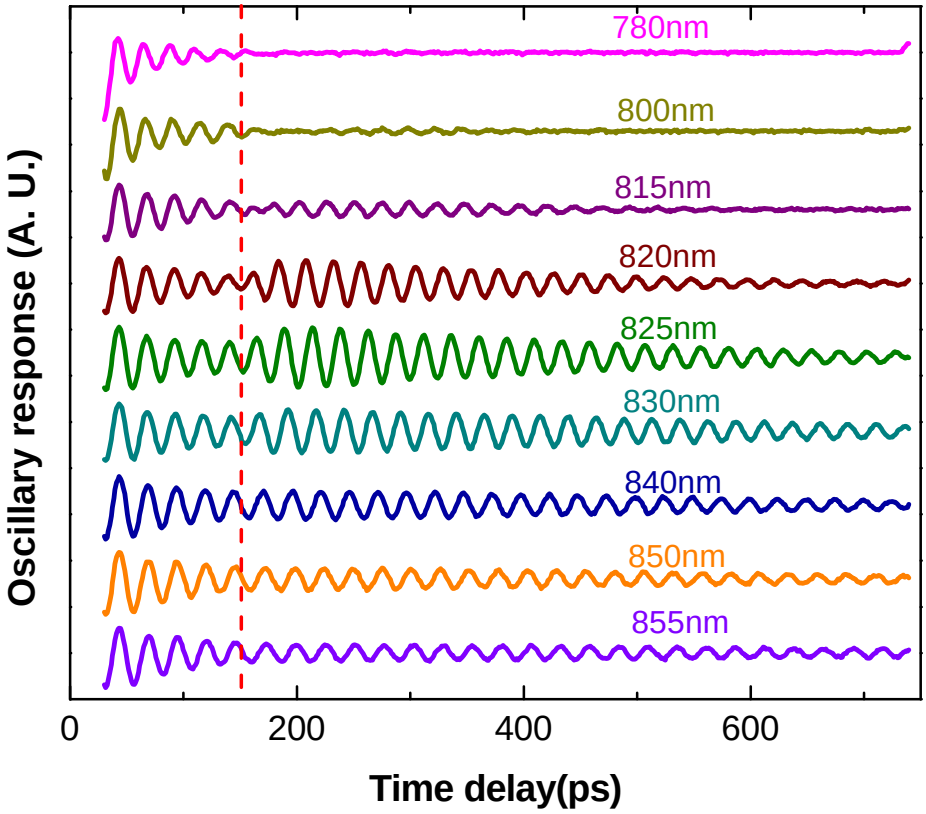

Figure 7.4. Oscillatory responses at different wavelengths with 500 nm GaSb top layer. The dash line indicates when the strain wave travels from GaSb layer into GaAs substrate.[48]

GaSb/GaAs with a 500 nm thick GaSb top layer over a variety of wavelengths. The pump light still generates the traveling CLAP wave in GaSb. However, since the GaSb layer is thick, the generated CLAP wave is seen to travel through GaSb before it reaches the GaAs. The speed of LA phonons in GaSb at 30 K is 4.01×10^3 m/s [60]. It can be calculated that it takes about 120 ps for the strain wave to reach GaAs. At the GaSb/GaAs interface, most of the acoustic phonon wave enters GaAs; with less than 1% of the

phonon energy reflected back[61]. We then ignore the reflected wave and assume the CLAP wave enters GaAs without loss.

The time that the phonon wave arrives at the interface is indicated by the red dash line in Fig. 7.4. This line separates the observed responses into two regimes. Before the red dash line, the CLAP wave propagates in the GaSb layer and produces oscillations as well. The amplitude of the oscillations damps relatively fast due to the absorption of probe light in GaSb. We have mentioned that the bandgap of GaSb is much smaller than the whole probe photon energy range, which accounts for the observed strong absorption. Responses in this regime are essentially wavelength independent. After the red dash line, the CLAP wave passes the GaSb/GaAs interface and continues to travel in the GaAs layer. The observed responses resemble results in the thin GaSb/GaAs sample, with strong wavelength dependence similar to what was demonstrated in Fig. 7.2. The lack of oscillations after the phonon wave enters GaAs at shorter wavelengths is due to strong absorption of both GaSb and GaAs. Although the two materials have different indices of refraction and speed of sound values, the oscillation periods calculated from Eq. 5.5 are very similar and cannot be distinguished from the experiment.

Interestingly, at the GaSb/GaAs interface, the oscillation amplitudes suddenly increase at wavelengths near the bandgap of GaAs in Fig. 7.4. The probe light intensity does not change abruptly across the interface. The intensity of the strain wave is material property related and does not have any probe light wavelength dependence. However, from the experimental results and the above analysis on the first sample, we know that strain wave induced change of the index of refraction, and hence the oscillation amplitude Eq. (5.13), has sharp wavelength dependence and peaks near the bandgap of GaAs. Thus,

this sudden increase of oscillation amplitude in Figure 7.4 is associated with the wavelength dependent change of the dielectric constant in GaAs, compared to GaSb where the light wavelength is always far from the bandgap energy. It is worth pointing out that this sudden change of amplitude can be utilized to determine unknown film thickness, by simply calculating the propagating distance from the measured oscillatory responses, providing the speed of sound is known.

A two-color[62] experiment was performed to corroborate the idea that the pump wavelength only creates the CLAP wave and does not play a direct role in the oscillations themselves. The laser light was tuned to 810 nm and a BBO crystal[63] was used to double the frequency (half the wavelength) of the pump beam while leaving the probe beam at the original frequency. After subtracting the thermal relaxation background and fitting the data with an exponentially damped oscillation function, we found, using the two color experimental configuration, a period of oscillation of about 23.9 ps. A single color experiment showed an almost identical value of about 23.8 ps. Such a drastic change in the pump beam from 810 nm to 405 nm should produce a very pronounced difference if the oscillations were a result of the pump beam. This supports the idea that the probe beam is responsible for the oscillations that we observe and not the pump beam.

In summary, we have carried out a systematic wavelength dependent study of traveling CLAP waves in the GaSb/GaAs system. Oscillatory responses from time-resolved pump-probe reflectance measurements can be observed in both GaSb and GaAs and are attributed to the interference of different reflected probe beams due to a moving 'Fabry-Perot' interferometer configuration. The oscillation period is determined by the probe wavelength and by material properties, such as the index of refraction and the

speed of LA phonons. We have focused our study mainly on GaAs, an important material both for research and application. This is the first detailed study of CLAP waves in GaAs. From our experimental results, the pump induced CLAP wave can last for at least 1 ns, and travels as deep as 5 μm. We have not only confirmed the model proposed by C. Thomsen *et al.*,[46] but also demonstrated the damping and amplitude change with probe wavelength near the bandgap of GaAs. We have also analyzed situations when the CLAP wave travels through a materials interface. For GaSb/GaAs interface, the strain pulse remains essentially unchanged and passes the interface without significant reflection or dephasing. This technique holds great promise, and will be shown in a later section, to be utilized as a non-invasive tool to measure depth-dependent film thicknesses and optical properties.

Using Metal Films to Probe GaAs Substrates

Metal-semiconductor contacts are important in all semiconductor devices. Depending upon the properties of the metal and the semiconductor, the contact between the two materials could be ohmic or rectifying (schottky-like) (see Appendix C). The long-lived nature of the strain wave makes it ideal to probe deep inside a semiconductor device. If a given metal layer on a semiconductor could create this strain wave, then this could provide an ideal way of probing semiconductor devices while still allowing an electric contact on the surface of the device.

In previous experiments, a thin GaSb layer was used to absorb the laser light and produce the strain wave that propagates at the speed of sound through the sample. Now

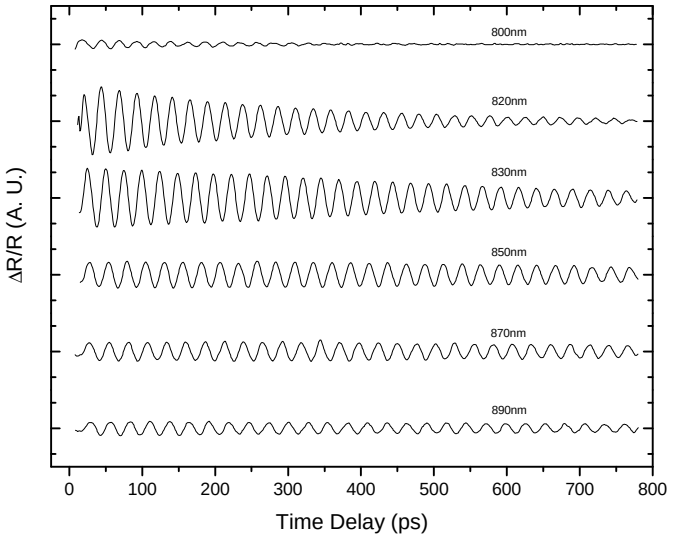

Figure 7.5. Typical differential reflection measurements performed on Al/GaAs.[64]

consider a 20 nm layer of aluminum that is deposited on a GaAs substrate. The purpose of the Al layer is to produce the strain wave just as the GaSb layer did previously. The deposition of the Al layer was not performed insitu. Therefore, there is probably a thin layer of oxide between the GaAs substrate and the deposited Al.[8] The differential reflection measurements are shown in Figure 7.5. As the figure shows, very strong coherent acoustic phonons are created in the Al and travel into the GaAs substrate. Great care needs to be taken when depositing the Al layer. If the aluminum layer is too thin (= 5 nm), there is little or no phonon generation in the aluminum and the only effect that is seen comes from the GaAs substrate. If the aluminum layer is too thick (> 40 nm), the probe will not penetrate through the Al layer and into the GaAs substrate.

In such a case the pump light would be incident on the sample, transferring energy to the conduction electrons in the Al film. The energy absorbed from the pump

light pulse is transferred to the conduction electrons in the metal. When the stress relaxes, the strain pulse would be directed towards the interface with the GaAs. Unlike the case of the GaSb/GaAs interface, the Al/GaAs interface is not acoustically matched. Therefore, the pulse will bounce back and forth within the Al film, undergoing partial transmission into the GaAs each time it reaches the Al/GaAs interface. The amount that the acoustic wave is reflected is given by the reflection coefficient[57]

$$r_{ac} = \frac{\left(Z_s - Z_f\right)}{\left(Z_s + Z_f\right)} \qquad 7.1$$

where Z_s and Z_f are the acoustic impedances (equal to the product of density and sound velocity) of the substrate and the film, respectively. At the free surface of the film the acoustic wave is totally reflected with a sign change. Successive oscillations of the strain thus have amplitude reduced by a factor r_{ac}. For the Al/GaAs interface, the reflection coefficient is approximately 0.18. As a result, the strain pulse that enters the GaAs would be made up of a few components. However, approximately 82% of the strain wave makes it into the GaAs substrate on the first pass. Therefore, the strain wave has only a slightly more complicated shape. By examining the data in Figure 7.5, one cannot distinguish between these oscillations and ones produced in a system that has two layers that are more acoustically matched. So it is reasonable to consider the strain wave as a single pulse of strain and neglect the affects of the subsequent reflections of the strain.

By depositing 20 nm of aluminum on the surface of a GaAs substrate, it allows the use of CLAP waves to probe into the GaAs substrate. However, because the Al and

the GaAs are not acoustically matched, the shape of the stain wave in the GaAs substrate takes on a slightly more complicated shape compared to the production of the CLAP waves in the GaSb/GaAs system.

Using Germanium to Probe Silicon Wafers

One possibility is the integration of this technique into the current silicon technology. This would open up the possibility of using CLAP waves to probe Si wafers for defect or impurity layers. However, CLAP wave production in silicon is not detectable. This is because the efficiency of electron-hole excitation in silicon, being an indirect bandgap semiconductor, is greatly reduced compared to a direct bandgap semiconductor like GaSb. The production of the CLAP wave is due to electron-phonon

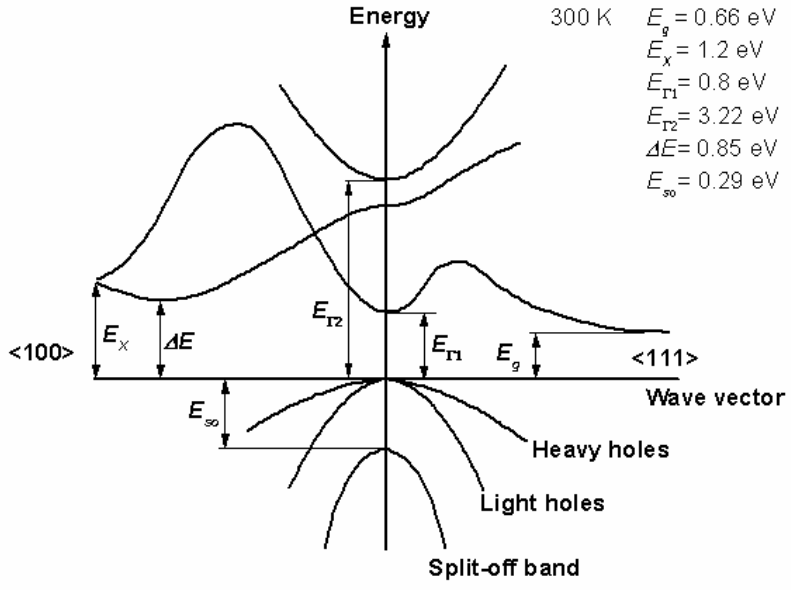

Figure 7.6. Band structure of Germanium.

scattering. If there are fewer electrons then less energy will be transferred to the lattice. This will cause a reduction in the amplitude of the strain wave beyond detectable limits.

One solution to this problem would be to grow epitaxial germanium layers on a bulk silicon wafers. Germanium is also an indirect semiconductor. However, the photon energy of the Ti:Sapphire laser can access the first direct band (E_{G1}) (Figure 7.6).[65]

Epitaxial growth of Ge on Si is not straightforward because of the large lattice mismatch (4%) between Ge and Si, which limits the quality of the epitaxial growth. Such growth of Ge on Si has large surface roughness. This can lead to degradation in device properties.

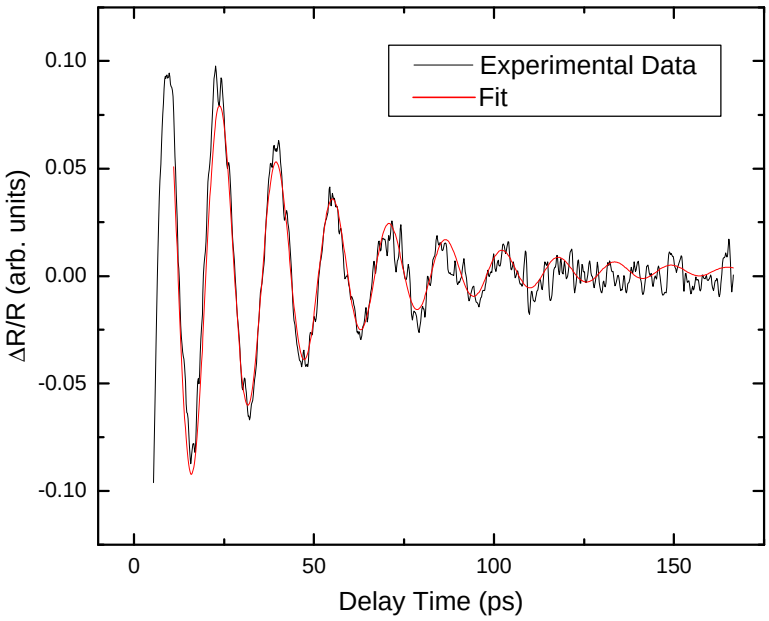

Figure 7.7. Oscillations produced in a Ge substrate (black curve). The red curve is a fit using the damped oscillation model.[64]

Thick 200 nm layers of epitaxial Ge have been successfully grown on standard bulk silicon wafers[66]. Hydrogen annealing of these types of samples have shown approximately 90% reduction of the surface roughness at 825 ºC. Smoother surfaces allow for better fabrication of devices. Successful growth of Ge on Si allows subsequent growth of optically active material such as GaAs since Ge and GaAs have nearly identical lattice constants.[67]

Figure 7.7 shows the differential reflectivity measurements for an undoped Ge sample. This measurement was taken at room temperature with 740 nm laser light. With this photon energy, we were able to access the first direct band in Ge and produce very strong oscillations in the differential reflectivity measurements. This shows that it is possible to excite CLAP waves directly in a Ge sample. Therefore, if a thin layer of Ge were grown on a Si wafer, the CLAP wave could be produced in Ge and then travel into the Si substrate. The CLAP wave could then be used to probe defects and impurities of the Si wafer as a function of depth.

Probing Buried Layers in GaAs

As seen in the previous sections, the traveling CLAP wave differentially samples the material as it proceeds from material to material across interfaces and it constitutes a promising non-invasive technique for measuring optical properties of the material as a function of depth. It is also a useful tool for measuring layer thicknesses and band gap energies.

This technique should be able to probe buried layers that exist deep inside a sample. These buried layers could consist of a doping layer, damage, impurities, or a thin

intervening layer. This pump-probe technique should give layer thickness as a function of depth with ultra-high resolution. To test if this is possible, a sample that is shown in Figure 7.8 was grown to see if this technique could probe the buried layer of $Ga_xIn_{1-x}As$. Using the Ti:Sapphire laser, a wavelength of light can be produced that is relatively transparent to the 500nm GaAs layer and to the GaAs substrate, while at the same time be absorbed in the $Ga_xIn_{1-x}As$ layer. The bandgap of unstrained $Ga_xIn_{1-x}As$ is given by[68]

$$E_g(x) = 0.4105 + 0.6337x + 0.475x^2. \qquad 7.2$$

One thing to note is that all wavelengths that are produced by the Ti:Sapphire laser are absorbed by the GaSb layer. This allows the generation of the CLAP wave in the GaSb layer at all wavelengths. At low temperatures (30 K) the bandgap of GaAs is approximately 817 nm (1.518 eV). By tuning the laser's wavelength above 817 nm, the 500 nm GaAs layer is now transparent to the light.

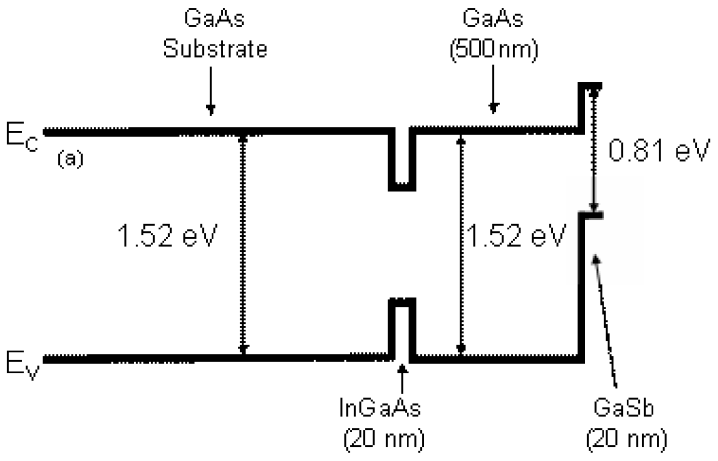

Figure 7.8. Simplified band structure of a GaSb/GaAs/$Ga_xIn_{1-x}As$/GaAs sample.

When the pump laser light is incident upon the sample, the CLAP wave is generated in the GaSb. It then travels at the speed of sound through the 500 nm GaAs layer. Since the wavelength of laser light is tuned above 817 nm (below the energy bandgap of GaAs) the oscillations for this layer should have relatively constant amplitude, because the probe light is not being absorbed by the sample. As the CLAP wave enters the $Ga_xIn_{1-x}As$ layer, the longitudinal sound velocity and the index of refraction in the $Ga_xIn1_{-x}As$ layer are different than in the GaAs layer. As a result of different material properties going from the GaAs layer into the $Ga_xIn_{1-x}As$ layer, there will be a phase change in the differential reflectivity signal. After the CLAP wave and the probe light exits the $Ga_xIn_{1-x}As$ layer, there should be another phase change going back into the GaAs layer.

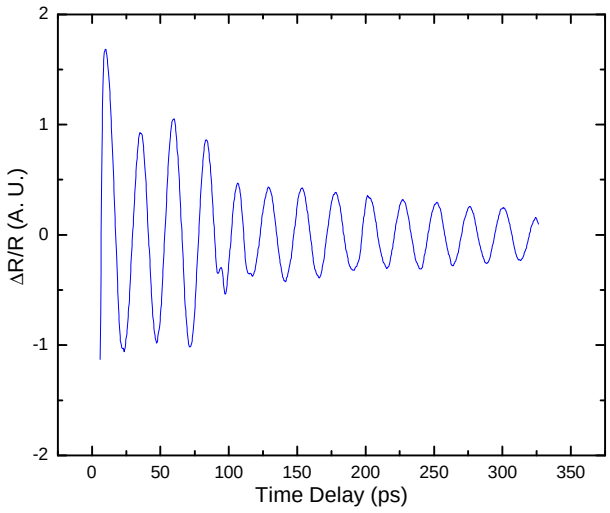

Figure 7.9. Differential reflection measurement at 825nm on GaSb(20nm)/GaAs(500nm)/$In_{0.50}Ga_{0.50}As$(20nm)/GaAs.[69]

A typical differential reflectivity measurement for a GaSb/$Ga_xIn_{1-x}As$/GaAs sample is shown in Figure 7.9. There is a phase change at approximately 91.2 ps and at 97.4 ps. This phase change indicates the delay time at which the CLAP wave enters and exits the $Ga_xIn_{1-x}As$ layer, respectively. Using the longitudinal sound velocity[65] in $Ga_xIn_{1-x}As$, the width of this layer can now be calculated to be approximately 25.5 nm. The growers of this sample were able to indirectly determine the layer thickness. Using x-ray diffraction (XRD) to determine the lattice constant and knowing the growth rate, they were able to determine the actual In concentration was 68% and the layer thickness was approximately 26.8 nm. This is very close to our measured value of the layer thickness that we reported. The depth of this layer from the surface can also be calculated by examining the oscillations before the phase shift and using the speed of sound in GaAs.[59] This distance is found to be approximately 400 nm.

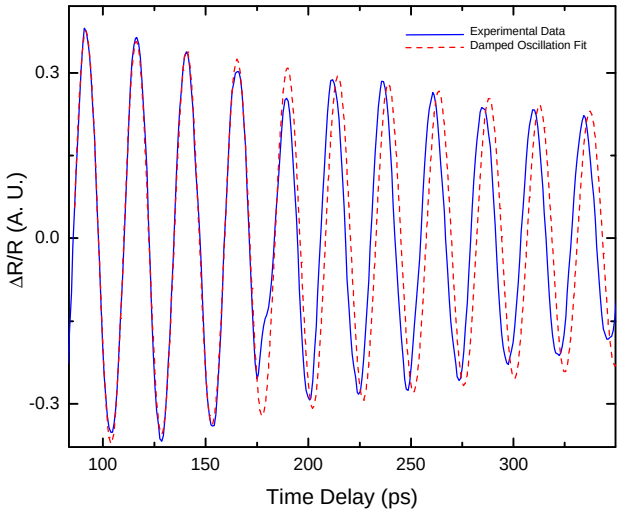

Figure 7.10. Differential reflection measurement at 825nm on GaSb(20nm)/GaAs(1000nm)/$In_{0.50}Ga_{0.50}As$(50nm)/GaAs.[69]

Another sample with a buried absorbing layer was also examined. This sample has the same basic structure as shown in Figure 7.9. However, now the MBE grown GaAs is suppose to be approximately 1000 nm thick and the $Ga_xIn_{1-x}As$ layer approximately 50 nm thick. The oscillatory response is shown in Figure 7.10. The blue solid line is the experimental data. The red dashed line is a damped oscillation function that is fit to the experimental data before the phase shift and then extended beyond the phase shift. From the damped oscillation fittings, this phase shift is approximately 28.59º. From the next section, we can express this phase shift, $\Delta\theta$, by taking the difference between the phase before the absorbing layer and after the absorbing layer. This can be expressed in terms of the delay time where the CLAP wave enters, t_1, and exits, t_2, the absorbing layer by

$$\Delta\theta = \frac{4\pi(n_2 v_2 - n_1 v_1)(t_2 - t_1)}{\lambda} \qquad 7.3$$

where n_i is the index of refraction and v_i is the longitudinal sound velocity in material i. Using Eq. 7.3, the time that the CLAP wave travels in the absorbing layer is calculated to be approximately 16.8 ps. Knowing the longitudinal sound velocity in $Ga_xIn_{1-x}As$, the width of this layer can be calculated to be 69.2 nm. The growers determined this layer thickness to be 68.9 nm, which is comparable to our measured thickness

In summary, we have probed different layers of $Ga_xIn_{1-x}As$ that have been buried in GaAs. We are able to identify the different layer thicknesses and the depth at which these layers are from the surface. This technique exhibits exceptional promise to be utilized as a non-invasive tool to measure layer thicknesses as a function of depth.

Modeling the CLAP Wave Behavior

To model the behavior of the CLAP waves in the samples in the previous section, we start with a very simple case. This would be when the CLAP wave is still located in Region I and has not reached the absorbing layer (Figure 7.11 (a)). Typically we have used a $Ga_xIn_{1-x}As$ layer as the absorbing layer. We can assume that the thin film on the surface and the CLAP wave both are infinitely thin. We also assume that there is no mixing at the boundaries between the different layers. In this case, we will consider the electric fields E_1 and E_2 that result from the reflections from the free surface and from the

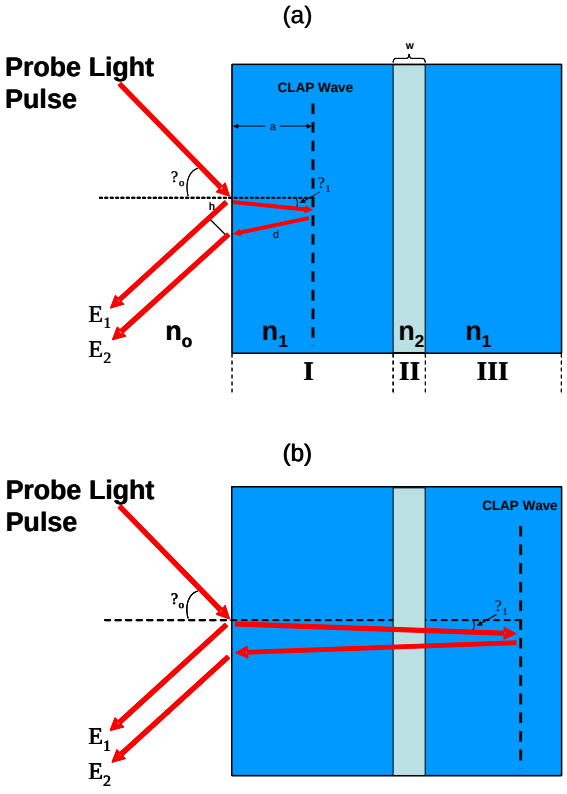

Figure 7. 11. (a) A schematic diagram of the CLAP wave located in Region I and (b) after it has passed through Region I and II and is located in Region III.

CLAP wave, respectively. The phase difference can be derived by examining the path difference between E_1 and E_2. For the case shown in Figure 7.11 (a), E_1 becomes

$$\boldsymbol{E}_1 = \boldsymbol{A}_1 cos\left(\frac{2\pi \boldsymbol{h}\boldsymbol{n}_o}{\lambda}\right). \qquad 7.4$$

The assumption can be made that h is constant and does not vary as the CLAP wave travels through the sample because the angle θ_1 is small.

In general, the electric field can be written as $E(t) = \cos(\omega t + kz)$. However, Eq. 7.4 only contains the phase term. We can leave out the frequency term because ω is constant in all the materials and when the intensity is calculated, this term drops out. We can also write

$$E_1 = A_1 e^{i\phi_o} \qquad 7.5$$

where $\phi_o = \frac{2\pi h n_o}{\lambda}$ is the phase term. From the assumption that h is constant, we can conclude that E_1 is also a constant.

The part of the probe beam that reflects from the CLAP wave, E_2, becomes

$$\mathbf{E}_2 = \mathbf{A}_2 e^{\left(i\frac{2p(2\mathbf{d})\mathbf{n}_1}{l}\right)} = \mathbf{A}_2 e^{\left(i\frac{4p\mathbf{n}_1\mathbf{v}_1\mathbf{t}}{l}\right)} \qquad 7.6$$

where n_1 and v_1 are the index of refraction and the longitudinal sound velocity of the material located in Region I, respectively. As the CLAP wave progresses, it will eventually encounter the absorbing layer (Region II) and then enter the substrate material (Region III) (Figure 7.11 (b)). Since the angle θ_1 is small, we neglect the refraction at the absorbing layer interfaces. Now E_2 needs to be broken into a piecewise function that takes into account the indices of refraction and the phonon velocities in each layer. Also the absorption of each layer needs to be taken into consideration. If we define t_1 and t_2 as the times where the absorbing layer begins and ends, respectively, then E_2 takes the form

$$\mathbf{E_2^I} = \mathbf{A}_2 e^{\left(i\frac{4\pi \mathbf{n_1 v_1 t}}{\lambda}\right)} e^{-2(\alpha_1 \mathbf{v_1 t})}; \quad 0 \le t < t_1, \tag{7.7}$$

$$\mathbf{E_2^{II}} = \mathbf{A}_2' e^{\left[i\frac{4p}{l}(\mathbf{n_1 v_1 t_1 + n_2 v_2 (t-t_1)})\right]} e^{-2(\mathbf{a_1 v_1 t_1 + a_2 v_2 (t-t_1)})}; \quad t_1 \le t < t_2, \tag{7.8}$$

$$\mathbf{E_2^{III}} = \mathbf{A}_2 e^{\left[i\frac{4p}{l}(\mathbf{n_1 v_1 t_1 + n_2 v_2 (t_2-t_1) + n_1 v_1 (t-t_2)})\right]} e^{-2(\mathbf{a_1 v_1 t_1 + a_2 v_2 (t_2-t_1) + a_1 v_1 (t-t_2)})}; \quad t_2 \le t \tag{7.9}$$

The total intensity from the interfering reflected beams can be calculated from Eq. 7.6 and Eq. 7.7 – 7.9 as follows

$$I(t) = \left|E_1(t) + E_2(t)\right|^2. \tag{7. 10}$$

Using this simple model, we can plot I(t) of the interfering electric fields with an absorbing layer buried in the substrate (Figure 7.12). This figure looks remarkably like the experimental data that is shown in Figure 7.9. One important feature that can be observed in our model (and in our experimental data) is a small peak that causes a phase change in our signal. This phase change is due to the different absorbing layer's parameters from GaAs, such as the thickness of the layer, the index of refraction, and the longitudinal sound velocity. In this model, the phase change is very sharp. This can be attributed to the assumption that we have perfect interfaces. In reality, the interfaces are not perfect and have some mixing. This mixing of the interfaces should smooth out this sharp feature. Another feature is the amplitude reduction due to the probe light being absorbed by the $In_xGa_{1-x}As$ layer. The use of this model will possibly allow insight into this CLAP wave technique that is not possible with the experimental data alone.

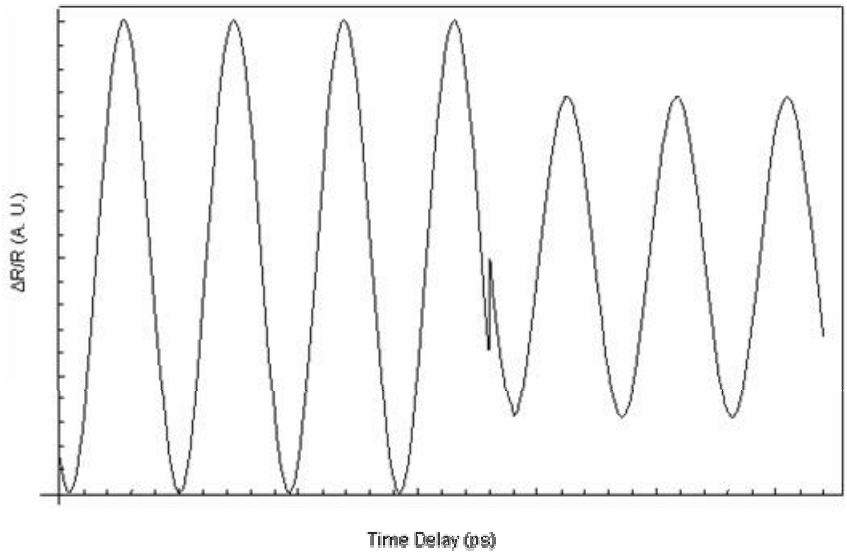

Figure 7.12. Oscillations due to the interference between E_1 and E_2. There is a phase change that is associated with a buried the $Ga_xIn_{1-x}As$ absorbing layer.[69]

Potential Applications

Due to the depth profiling aspects of the CLAP technique, there are a few possible applications that should be pursued. The first possible application is the use of this technique to identify different doping levels in different layers in a silicon wafer. If the top layer in a Si wafer is n-doped with arsenic to a level of 10^{19} cm^{-1} and just beneath that there is a layer p-doped with boron to a level of 10^{17} cm^{-1}, then there should be a difference in the bandgap of the two layers due to the carrier concentration. This difference could be as large as 60 meV.[6] We have seen that around the bandgap the oscillation amplitude increases due to the change in the dielectric function. Therefore, this technique should be able to distinguish between these two layers because each layer should have different bandgap energies.

Another possible application would be to use this technique in conjunction with an Atomic Force Microscope (AFM). By shining laser light on an AFM tip that is close to the surface of the sample (thus making an apertureless SNOM), a CLAP wave will be produced that has hemispherical symmetry. As this wave propagates through the sample, it could encounter different structures such as defects, voids, interfaces, or nanoparticles. If these structures are not acoustically matched with the surrounding material, part of the strain wave will be reflected. When the reflected strain wave approaches the surface, it will cause a slight deformation that could be detected using another AFM tip. Knowing the time the strain wave started in the material, it could be deduced where this structure is located inside the sample.

Instead of using laser light to excite the sample and produce a CLAP wave, ion beams could also be used. As the ion penetrates into the sample it will produce electron-

hole pairs along its path. Now the CLAP wave will have cylindrical symmetry which could be used for different applications.

One could also use CLAP waves to probe semiconductors for interface roughness or for damage. Either case would presumably modulate the optical and mechanical properties of the semiconductor locally and allow this CLAP wave technique to distinguish between these layers and give information about these layers as a function of depth.

The versatility of this technique makes it ideal to examine many different systems in different configurations. Using CLAP waves in any of these configurations is a rich tool that gives a wealth of information on the optical properties of the sample along with information on defects, nanoparticles, interfaces, and even doping levels as a function of depth.

CHAPTER VIII

SUMMARY

In this dissertation, we applied tunable, ultra-fast lasers along with a pump-probe experimental technique to study electron and phonon dynamics. With one channel, Second Harmonic Generation can be monitored, which is a contactless and non-invasive probe that provides time resolved information on carrier dynamics and transport near interfaces. With another channel, differential reflectivity can be monitored, which gives information on carrier dynamics in the bulk, in our particular case the coherent longitudinal acoustic phonons as they travel into the sample.

We have studied the ultra-fast dynamics of interfacial electric fields in GaAs/GaSb and GaAs/GaSb/InAs heterostructures using a pump-probe SHG technique. We observed a complicated evolution of the interfacial fields originating from the redistribution of carriers between the interfaces. The ability of the EFISH signal to monitor spatially separated regions makes pump-probe SHG a unique tool for studying relaxation and transport phenomena in multilayer semiconductor structures.

We have carried out a systematic wavelength dependent study of traveling CLAP waves in the GaSb/GaAs system. Oscillatory responses from time-resolved pump-probe reflectance measurements can be observed in several semiconducting materials, including GaAs, GaSb, and Ge, and are attributed to the interference of different reflected probe beams due to a moving ‘Fabry-Perot’ interferometer configuration. The oscillation period is determined by the probe wavelength and by material properties, such as the index of

refraction and the speed of LA phonons. We have focused our study mainly on GaAs, an important material both for research and application. This is the first detailed study of CLAP waves in GaAs. From our experimental results, the pump induced CLAP wave can last for at least 1 ns, and travels as deep as 5 μm. We have not only confirmed the model proposed by C. Thomsen *et al*.,[46] but also demonstrated the damping and amplitude change with probe wavelength near the bandgap of GaAs. We have also analyzed situations when the CLAP wave travels through a materials interface. For the GaSb/GaAs interface, the strain pulse remains essentially unchanged and passes the interface without significant reflection or dephasing.

We have produced CLAP waves in different materials like aluminum and germanium. The production of strain waves in aluminum is very promising because this technique can now be used to probe any semiconductor device that has a thin metal contact like aluminum. The production of strain waves in germanium is exciting because it can be used to access silicon devices. Both of these materials can be utilized to integrate the depth profiling aspects of the CLAP wave technique with the current silicon technology.

We have also studied GaSb/GaAs/$In_xGa_{1-x}As$/GaAs heterostructures using the CLAP wave technique. By examining the phase change due to the CLAP wave changing velocity and the probe light changing velocity, the width of the buried $In_xGa_{1-x}As$ can be determined. Also, by examining the oscillations before the phase change, the depth of this layer with respect to the surface of the sample can be extracted. This shows that this technique holds great promise to be utilized as a non-invasive tool to measure depth-dependent film thicknesses, optical properties and ultimately depth profiles.

Starting with some very simple assumptions, a model has been developed that satisfactorily characterizes our experimental results. This model contains two very important features. The first feature is a phase shift due to the change in the material properties as the CLAP wave moves inside the absorbing layer. The second important feature is the amplitude reduction when the probe photon energy is larger than the bandgap of the absorbing layer. Both features can be utilized in future applications of depth profiling technique using CLAP waves.

APPENDIX

A. MATERIAL PROPERTIES OF GaAs and GaSb

Table A.1. Material Properties of GaAs and GaSb[6,65]

Properties	GaAs	GaSb
Crystal structure	Zinc Blende	Zinc Blende
Lattice constant (Å)	5.6533	6.0959
Density (g/cm^3)	5.32	5.61
Dielectric constant	13.1	15.7
Intrinsic Carrier Concentration (cm^{-3})	1.79×10^6	1.5×10^{12}
Breakdown field (V/cm)	~4×10^5	~5×10^4
Energy gap (eV) at 300 K 30 K 4.3 K	 1.424 1.517 1.519	 0.727 0.810 0.813
Linear coefficient of thermal expansion ($°C^{-1}$)	6.86×10^{-6}	7.75×10^{-6}
Electron affinity, ? (eV)	4.07	4.06
Acoustic Wave Speeds (m/s) longitudinal transverse	 4.73×10^3 3.35×10^3	 3.97×10^3 2.77×10^3

B. MATERIAL PROPERTIES OF SILICON, GERMANIUM, AND $Al_xGa_{1-x}As$

Table B.1. Properties of Silicon, Germanium, and $Al_xGa_{1-x}As$. [6,65]

Properties	Silicon	Germanium	$Al_xGa_{1-x}As$
Crystal structure	Diamond	Diamond	Zinc Blende
Lattice constant (Å)	5.43095	5.64613	5.6533+0.0078x
Density (g/cm^3)	2.328	5.3267	5.32 – 1.56x
Dielectric constant	11.9	16.0	12.90-2.84x
Intrinsic Carrier Concentration (cm^{-3})	1.45×10^{10}	2.4×10^{13}	x=0.1 2.1×10^5 cm^{-3} x=0.3 2.1×10^3 cm^{-3} x=0.5 2.5×10^2 cm^{-3} x=0.8 4.3×10^1 cm^{-3}
Breakdown field (V/cm)	$\sim 3 \times 10^5$	$\sim 10^5$	
Energy gap (eV) at 300 K 30 K 4.3 K	 1.125 1.169 1.170	 0.661 0.740 0.742	$E_g = E_g(0) - \frac{5.41 \cdot 10^{-4} T^2}{(T+204)}$ where $E_g(0) = 1.519 + 1.155x + 0.37x^2$
Linear coefficient of thermal expansion ($°C^{-1}$)	2.6×10^{-6}	5.8×10^{-6}	$(5.73-0.53x) \times 10^{-6}$
Electron affinity, ? (eV)	4.03	4.0	4.07-1.1x (x<0.45) 3.64-0.14x (x>0.45)
Acoustic Wave Speeds (m/s) longitudinal transverse	 8.43×10^3 5.84×10^3	 4.87×10^3 3.57×10^3	 $4.73+0.68x+0.24x^2$ $3.34+0.46x+0.16x^2$

C. METAL-SEMICONDUCTOR CONTACTS

To make an ideal metal-semiconductor (MS) contact,[7] we assume three conditions: (1) The metal and semiconductor are in intimate contact on an atomic scale, with no layers of any type (such as an oxide) between the components. (2) There is no interdiffusion or intermixing of the metal and semiconductor. (3) There are no absorbed impurities or surface charges at the MS interface.

There are several terms that need to be introduced using Figure C.1 to analyze the MS contacts. The dashed line at the top of the figure denotes the minimum energy an electron needs to free itself from the material and is called the vacuum level, E_0. The Fermi energy of the semiconductor is denoted by E_{FS}. The energy difference between the vacuum level and the Fermi energy is known as the workfunction, Φ. The metal workfunction, Φ_M, is an invariant fundamental property of the specified metal. The semiconductor workfunction, Φ_S, is described by

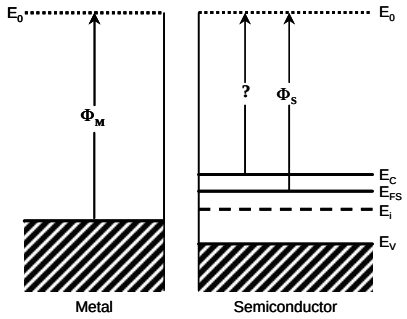

Figure C.1. Energy-band diagrams for a metal and *n*-type semiconductor that are electrically isolated.[7]

$$\Phi_S = c + \left(E_c - E_F\right)_{FB} \qquad \text{C. 1}$$

where the electron affinity, χ, is an invariant fundamental property of the specified semiconductor and is defined as

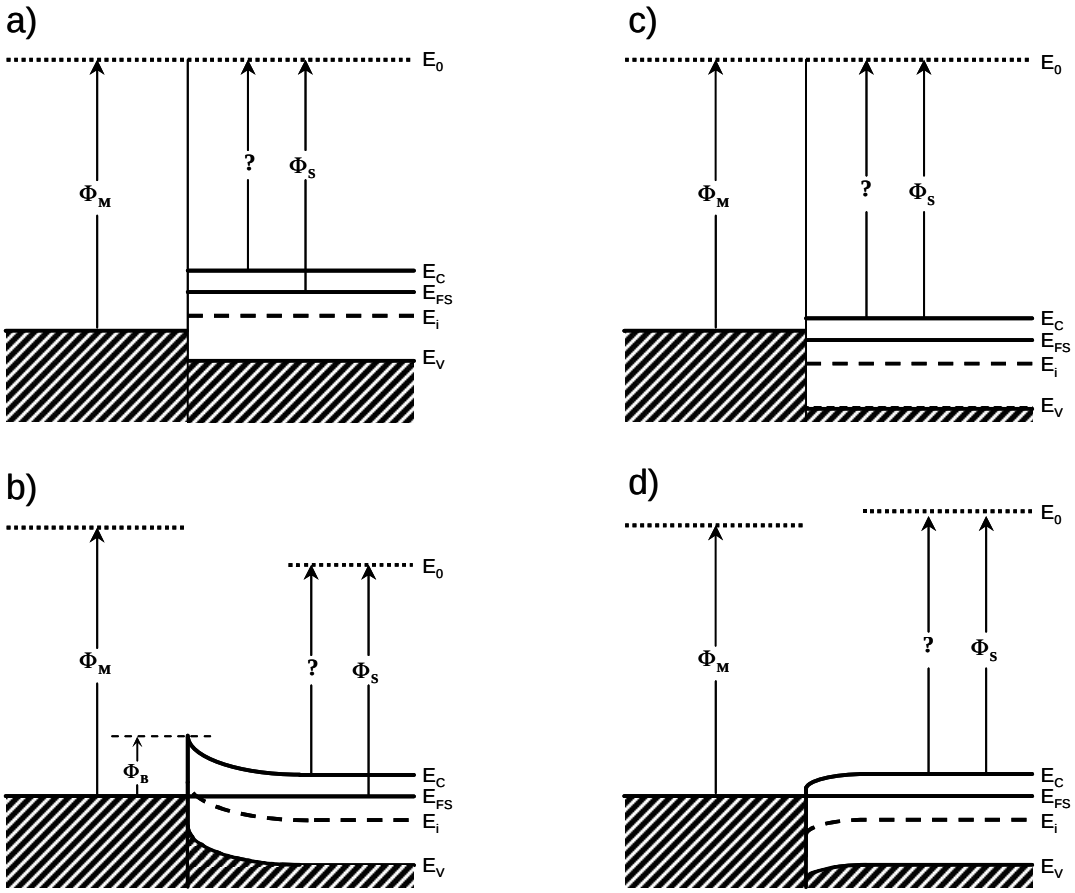

Figure C.2. Energy-band diagrams for ideal MS contacts between a metal and an n-type semiconductor: a) an instant after contact formation and b) under equilibrium for $\Phi_M > \Phi_S$ system; c) an instant after contact formation and d) under equilibrium for $\Phi_M < \Phi_S$ system.[7]

$$c \equiv (E_0 - E_c)\Big|_{surface} . \qquad \text{C. 2}$$

Now let the metal and the n-type semiconductor in Figure 1 ($\Phi_M > \Phi_S$) be brought into contact to form an ideal MS contact. An instant after contact the energy band diagram will look like Figure C.2(a). The energy band diagrams are drawn where the E_0 reference levels for each material are the same. Since the Fermi levels for the materials do not line up ($E_{FS} \neq E_{FM}$), the contact shown in Figure C.2(a) is not in equilibrium. Under equilibrium conditions the Fermi level in a material or a group of materials in intimate contact must be constant with position. The constancy of the Fermi level means that E_F is to appear as a horizontal line on equilibrium energy band diagrams. A short time after the contact is made, electrons will begin transferring from the semiconductor to the metal. The net loss of electrons from the semiconductor creates a surface depletion region and a growing barrier to electron transfer from the semiconductor to the metal. This will continue until there is a steady-state situation, where the transfer rate across the interface is the same in both directions and E_F is the same throughout the structure. As a result, the equilibrium energy band diagram for an ideal $\Phi_M > \Phi_S$ metal to n-type semiconductor contact is shown in Figure C.2(b). It should be emphasized that Φ_M and χ are material constants and remain unaffected by the contacting process. Therefore, the vacuum level will have the same shape as the conduction band. It is also important to note that for an ideal MS (n-type) contact

$$\Phi_B = \Phi_M - c \qquad \text{C. 3}$$

where Φ_B is the surface potential-energy barrier that is seen by electrons with E = E_F in the metal. If this entire argument is repeated for a metal and n-type semiconductor where

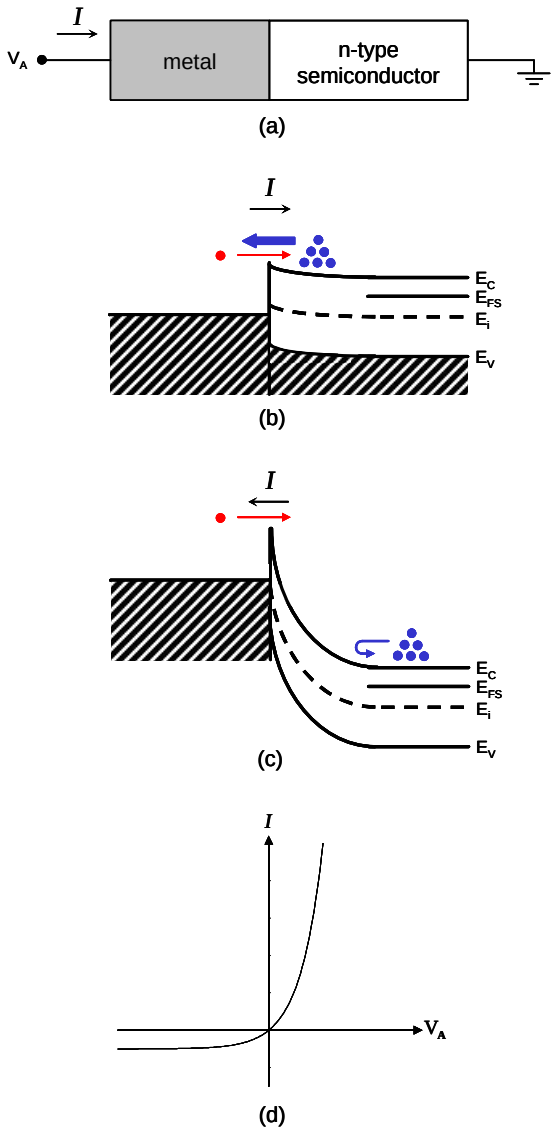

Figure C.3. Response of the $\Phi_M > \Phi_S$ (n-type) MS contact to an applied d.c. bias. (a) Definition of current and voltage polarities. Energy band diagram and carrier activity when (b) $V_A > 0$ and (c) when $V_A < 0$. (d) General form of the I-V characteristics of this system.[7]

$\Phi_M < \Phi_S$, one would arrive at the equilibrium energy band diagram shown in Figure C.2(d).

It is also important to consider the effect of biasing the two MS structures in Figure C.2. To apply the bias, the semiconductor is taken to be grounded and V_A is applied to the metal, as seen in Figure C.3(a). The current I is defined to be positive when current flows from the metal to the semiconductor.

With an n-type semiconductor, electron flow must be examined to determine whether the MS contacts are rectifying or ohmic. Consider first the MS contact where $\Phi_M > \Phi_S$. If $V_A > 0$ (forward bias) is applied, as shown in Figure C.3(b), E_{FM} is lowered below E_{FS}. This reduces the barrier seen by electrons in the semiconductor, and therefore permits a net flow of electrons from the semiconductor to the metal. If $V_A < 0$ (reverse bias) is applied, as shown in Figure C.3(c), E_{FM} is raised above E_{FS}. This increases the barrier seen by electrons in the semiconductor and blocks the flow of electrons from the semiconductor to the metal. Some electrons in the metal will be able to overcome the F_B barrier, but the associated reverse-bias current should be relatively small. Since the barrier that the electrons in the metal see is the same for all reverse biases, the reverse current is expected to remain constant after the reverse bias reaches a certain value. This type of MS contact is therefore rectifying.

The behavior for the $\Phi_M < \Phi_S$ MS contact to an applied bias is considerably different. Now there is no barrier at all, as seen in Figure C.2(d), for electron flow from the semiconductor to the metal. So even a small $V_A > 0$ (forward bias) gives rise to a large forward bias current. When $V_A < 0$ (reverse bias) is applied, there is a small barrier for electron flow from the metal to the semiconductor. This barrier essentially vanishes if

Table C.1. Electrical Nature of Ideal MS contacts.[7]

	n-type Semiconductor	p-type Semiconductor
$\Phi_M > \Phi_S$	Rectifying	Ohmic
$\Phi_M < \Phi_S$	Ohmic	Rectifying

the reverse bias exceeds a few tenths of a volt. With relatively small reverse biases, large reverse currents are expected that do not saturate. This type of behavior is not rectifying, but ohmic-like.

The conclusion is that an ideal MS contact formed from a metal and an n-type semiconductor will be a rectifying contact if $\Phi_M > \Phi_S$ and an ohmic-like contact if $\Phi_M < \Phi_S$. The same type of argument can be applied to an ideal MS contact formed from a metal and a p-type semiconductor. This will lead to the conclusion that the contact will be rectifying if $\Phi_M < \Phi_S$ and ohmic-like if $\Phi_M < \Phi_S$ (Table C.1).

D. ACOUSTO-OPTIC MODULATOR

An acousto-optic modulator[70] (AOM) is a device which allows control of the power, frequency or spatial direction of a laser beam with an electrical drive signal. It is based on the acousto-optic effect, i.e., the modification of the refractive index by the oscillating mechanical pressure of a sound wave. The key element of an AOM is a transparent crystal (or piece of glass) through which the light propagates (Figure D.1). A piezoelectric transducer attached to the crystal is used to excite a high-frequency sound wave (with a frequency in the order of 100 MHz). Light can then experience Bragg diffraction at the periodic refractive index grating generated by the sound wave; therefore, AOMs are sometimes called *Bragg cells*. The scattered beam has a slightly modified optical frequency (increased or decreased by the frequency of the sound wave) and a slightly different direction. The frequency and direction of the scattered beam can be controlled via the frequency of the sound wave, while the acoustic power allows control of the optical powers. For sufficiently high acoustic power, more than 50% of the optical power can be diffracted.

The acoustic wave may be absorbed at the other end of the crystal. Such a *traveling-wave geometry* allows to achieve a broad modulation bandwidth of many megahertz. Other devices are resonant for the sound wave, exploiting the strong reflection of the acoustic wave at the other end of the crystal. The resonant enhancement can greatly increase the modulation strength (or decrease the required acoustic power), but reduces the modulation bandwidth.

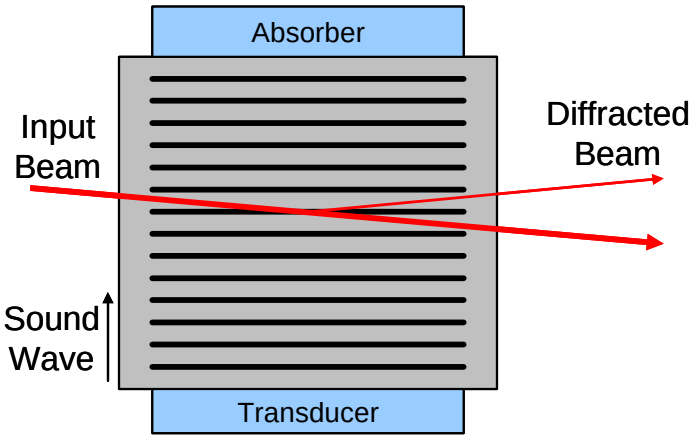

Figure D.1. Schematic setup of a non-resonant acousto-optic modulator. A transducer generates a sound wave, at which a light beam is partially diffracted. The diffraction angle is exaggerated.

Common materials for acousto-optic devices are tellurium dioxide, crystalline quartz, and fused silica. There are manifold criteria for the choice of the material, including the elasto-optic coefficients, the transparency range, the optical damage threshold, and required size.

Some applications of acousto-optic modulators are: (1) Q switching of solid state lasers (where the AOM, then called Q switch, typically serves to block the laser cavity before the pulse is to be generated), (2) active mode locking (where the AOM modulates the cavity losses with the round-trip frequency or a multiple thereof), (3) modulating the power of a laser beam, e.g. for laser printing, and as in our case (4) shifting the frequency of a laser beam, e.g. in various measurement schemes.

REFERENCES

[1] Femtosecond hole thermalization in bulk GaAs, R. Tommasi, P. Langot, and F.Vallee, Appl. Phys. Lett. **66**, 1361 (1995).

[2] J. Shah, *Ultrafast Spectroscopy of Semiconductors and Semiconductor Nanostructures*, Second Enlarged Edition, New York: Springer, 1999.

[3] Characterization of semiconductor interfaces by second-harmonic generation, G. Lupke, Surf. Sci. Rep. **35**, 75 (1999).

[4] Crystal structure and chemical constitution, V. M. Goldschmidt, Trans. Faraday Soc. 25, 253 (1929).

[5] H. Welker, Z. Naturforsch, Vol. A, No. 7, p. 744, 1952.

[6] S. M. Sze, *Semiconductor Devices Physics and Technology*, J. Wiley, New York, 1985.

[7] R. F. Pierret, *Semiconductor Fundamentals*, Addison-Wesley Publishing, New York, 1996.

[8] P. H. Holloway, *Handbook of Compound Semiconductors*, Noyes Publications, 1995.

[9] H. C. Casey, *Diffusion in III-V Compound Semiconductors, Atomic Diffusion in Semiconductors*, D. Shaw, Editor, Plenum, New York, 1973.

[10] Properties of Vacancy Defects in GaAs Single Crystals, S. Y. Chiang, J. Appl. Phys. **45**, 2986 (1975).

[11] S. Markram-Ebied, "Nature of EL2: The Main Native Midgap Electron Trap in VPE and Bulk GaAs," in *Semi-insulating III-V Materials*, D. C. Look, Editor, Shiva Publishing Ltd., England, 1984.

[12] Y. Nanishi, Jpn. J. Appl. Phys. **22**, (1983).

[13] Direct observation of dislocation effects on threshold voltage of a GaAs field-effect transistor, S. Miyazawa, Y. Ishii, S. Ishida, and Y. Nanishi, Appl. Phys. Lett. **43**, 853 (1984).

[14] The Influence of Dislocation Density on the Uniformity of Electrical Properties of Si Implanted, Semi-Insulating LEC-GaAs, T. Honda, Jpn. J. Appl. Phys. **22**, L270 (1983).

[15] R. S. Muller, T. I. Kamins, and M. Chan, *Device Electronics for Integrated Circuits*, John Wiley & Sons, 2003.

[16] Concentration dependence of the refractive index for n- and p-type GaAs between 1.2 and 1.8 eV, D. D. Sell, H. C. Casey, Jr., and K. W. Wecht, J. Appl. Phys. **45**, 2650 (1974).

[17] Polariton Reflectance and Photoluminescence in High-Purity GaAs, D. D. Sell, S. E. Stokowski, R. Dingle, and J. V. DiLorenzo, Phys. Rev. B **7**, 4568 (1973).

[18] Temperature Dependence of the Energy Gap in GaAs and GaP, M. B. Panish and H. C. Casey, Jr., J. Appl. Phys. **40**, 163 (1969).

[19] The Standard Thermodynamic Functions for the Formation of Electrons and Holes in Ge, Si, GaAs, and GaP, C. D. Thurmond, J. Electrochem. Soc. **122**, 1133 (1975).

[20] Temperature dependence of the energy gap in semiconductors, Y. P. Varshni, Physica **34**(1), 149 (1967).

[21] For a general reference see e.g. R. W. Boyd, *Nonlinear Optics*, Academic Press, 1992.

[22] C. Rulliere, *Femtosecond Laser Pulses*, Springer, 1998.

[23] Optical second-harmonic generation induced by a dc electric field at the Si-SiO_2 interface, O. A. Aktsipetrov, A. A Fedyanin, V. N. Golovkina, and T. V. Murzina, Opt. Lett, **19**, 1450 (1994).

[24] DC-electric-field-induced and low-frequency electromodulation second-harmonic generation spectroscopy of Si(001)-SiO_2 interfaces, O. A. Aktsipetrov, A. A Fedyanin, A. V. Melnikov, E. D. Mishina, A. N. Rubtsov, M. H. Anderson, P. T. Wilson, M. ter Beek, X. F. Hu, J. I. Dadap and M. C. Downer, Phys. Rev. B **60**, 8924 (1999).

[25] Characterization of multiple Si/SiO_2 interfaces in silicon-on-insulator materials via second-harmonic generation, B. Jun, Y. V. White, R. D. Schrimpf, D. M. Fleetwood, F. Brunier, N. Bresson, S. Cristoloveanu, N. H. Tolk, Appl. Phys. Lett **85**, 3095 (2004).

[26] Charge Trapping in Irradiated SOI Wafers Measured by Second Harmonic Generation, B. Jun, R. D. Schrimpf, D. A. Fleetwood, Y. V. White, R. Pasternak, S. N. Rashkeev, F. Brunier, N. Brsson, M. Fouillat, S. Cristoloveanu, N. H. Tolk, IEEE Transactions on Nuclear Science **51**, 3231 Part 2 (2004).

[27] R. Pasternak, B. Jun, R. D. Schrimpf, D. M. Fleetwood, M. L. Alles, R. P. Dolan, R. W. Standley, and N. H. Tolk, *Electrochemical Society Meeting, Silicon-on-Insulator Technology and Devices XII*, 383, May 2005.

[28] Ultrafast phenomena VIII, Edited by J. L. Martin Springer Series in Chemical Physics Springer, Berlin, 1993, Vol. 55.

[29] Femtosecond passively mode-locked Ti:Al_2O_3 laser with a nonlinear external cavity, J. Goodberlet, J. Wang, J. G. Fujimoto, and P. A. Schulz, Opt. Lett. **14**, 1125 (1989).

[30] 60-fsec pulse generation from a self-mode-locked Ti:sapphire laser, D. E. Spence, P. N. Kean, and W. Sibbett, Opt. Lett. **16**, 42 (1991).

[31] Self-starting 6.5-fs pulses from a Ti:sapphire laser, D. Jung, F. X. Kartner, N. Matuschek, D. H. Sutter, F. Morier-Genoud, G. Zhang, U. Keller, V. Scheuer, M. Tilsch, and T. Schudi, Opt. Lett. **22**, 1009 (1997).

[32] Adapted from the Ti:Sapphire Mira 900 manual.

[33] Influence of hot phonons on energy relaxation of high-density carriers in germanium, H. M. van Driel, Phys. Rev. B **19**, 5928 (1979).

[34] Electronic power transfer in pulsed laser excitation of polar semiconductors, W. Potz and P. Kocevar, Phys. Rev. B 28, 7040 (1983).

[35] Probing ultrafast carrier and phonon dynamics in semiconductors, A. Othonos, Appl. Phys. Rev. **83**, 1789 (1998).

[36] *Semiconductors Probed by Ultrafast Laser Spectroscopy*, Volumes I and II, edited by R. R. Alfano, Academic , New York, 1971.

[37] F. Wooden, *Optical Properties of Solids*, Academic, New York, 1972.

[38] J. I. Pankove, *Optical Processes in Semiconductors*, Dover, New York, 1971.

[39] Spectroscopy of Hot Carriers In Semiconductors, S. A. Lyon, J. Lumin. **35**, 121 (1986).

[40] Hot electrons and phonons under high intensity photoexcitation of semiconductors, J. Shah, Solid-State Electron. **21**, 43 (1978).

[41] Subpicosecond Time-Resolved Raman Spectroscopy of LO Phonons in GaAs, J. A. Kash, J. C. Tsang, and J. M. Hvam, Phys. Rev. Lett. **54**, 2151 (1985).

[42] B. R. Nag, *Theory of Electrical Transport in Semiconductors*, Pergamon, New York, 1972.

[43] K. Seeger, *Semiconductor Physics*, Springer, New York, Vol. 40, 1988.

[44] Correlation of hot-phonon and hot-carrier kinetics in Ge on a picosecond time scale, A. Othonos, H. M. van Driel, J. F. Young, and P. J. Kelly, Phys. Rev. B 43, 6682 (1991).

[45] H. J. Maris, in *Physical Acoustics*, edited by W. P. Mason and R. N. Thurston (Academic, New York, 1971), vol. 7, p.279.

[46] Surface generation and detection of phonons by picosecond light pulses, C. Thomsen, H. T. Grahn, H. J. Maris, and J. Tauc, Phys. Rev. B 34, 4129 (1986).

[47] M. Born, "Principles of optics : electromagnetic theory of propagation, interference and diffraction of light", 7th expanded ed., Cambridge ; New York : Cambridge University Press, 1999.

[48] Near-bandgap wavelength-dependent studies of long-lived traveling coherent longitudinal acoustic phonon oscillations in GaSb/GaAs systems, J. K. Miller, J. Qi, Y. Xu, Y. J. Cho, X. Liu, J. K. Furdyna, I. Perakis, T. V. Shahbazyan, and N. Tolk, Submitted to PRL.

[49] Generation and detection of coherent optical phonons in germanium, T. Pfeifer, W. Kutt, and H. Kurz, Phys. Rev. Lett. **69**, 3248 (1992).

[50] Coherent Acoustic Phonon Oscillations in Semiconductor Multiple Quantum Wells with Piezoelectric Fields, C. Sun, J. Liang, and X. Yu, Phys. Rev. Lett. **84**, 179 (2000).

[51] Long-lived coherent acoustic waves generated by femtosecond light pulses, I. Bozovic, M. Schneider, Y. Xu, R. Sobolewski, Y. H. Ren, G. Lupke, J. Demsar, A. J. Taylor, and M. Onellioni, Phys. Rev. B **69**, 132503 (2004).

[52] Ultrafast dynamics of coherent optical phonons and nonequilbrium electrons in transition metals, M. Hase, K. Ishioka, J. Demsar, K. Ushida, and M. Kitajima, Phys. Rev. B **71**, 184301 (2005).

[53] Coherent optical and acoustic phonon generation correlated with the charge-ordering phase transition in $La_{1-x}Ca_xMnO3$, D. Lim, V. K. Thorsmolle, R. D. Averitt, Q. X. Jia, K. H. Ahn, M. J. Graf, S. A. Truqman, and A. J. Taylor, Phys. Rev. B **71**, 134403 (2005).

[54] Propagating coherent acoustic phonon wave packets in $In_xMn_{1-x}As/GaSb$, J. Wang, Y. Hashimoto, J. Kono, A. Oiwa, H. Munekata, G.D. Sanders, and C. J. Stanton, Phys. Rev. B **72**, 153311 (2005).

[55] Long-lived, coherent acoustic phonon oscillations in GaN single crystals, S. Wu, P. Geiser, J. Jun, J. Karpinski, J.-R. Park, and R. Sobolewski, Appl. Phys. Lett. **88**, 041917 (2006).

[56] Probing strained InGaN/GaN nanostructures with ultrashort acoustic phonon wave packets generated by femtosecond lasers, J. S. Yahng, Y. D. Jho, K. J. Yee, E. Oh, J. C. Woo, D. S. Kim, G. D. Sanders, and C. J. Stanton, Appl. Phys. Lett. **80**, 4723 (2002).

[57] Phonon attenuation and velocity measurements in transparent materials by picosecond acoustic interferometry, H.-N. Lin, R. J. Stoner, H. J. Maris, and J. Tauc, J. Appl. Phys. **69**, 3816 (1991).

[58] Dielectric functions and optical parameters of Si, Ge, GaP, GaAs, GaSb, InP, InAs, and InSb from 1.5 to 6.0 eV, D. E. Aspnes and A. A. Studna, Phys. Rev. B **27**, 985 (1983).

[59] Semiconducting and other major properties of gallium arsenide, J. S. Blakemore, J. Appl. Phys. **53**, R123 (1982).

[60] Elastic constants and lattice anharmonicity of GaSb and GaP from ultrasonic-velocity measurements between 4.2 and 300 K, W. F. Boyle and R. J. Sladek, Phys. Rev. B **11**, 2933 (1975).

[61] A. Wood, *Acoustics*, Dover, New York, 1966.

[62] A pump-probe experiment is called two-color when the frequencies of the pump and probe are different.

[63] Optical, mechanical, and thermal properties of barium borate, D. Eimerl, L. Davis, S. Velsko, E. K. Graham, A. Zalkin, J. Appl. Phys. **62**, 1968 (1987).

[64] J. K. Miller, unpublished data.

[65] http://www.ioffe.rssi.ru/SVA/NSM/Semicond/GaInAs/mechanic.html

[66] Effects of hydrogen annealing on heteroepitaxial-Ge layers on Si: Surface roughness and electrical quality, A. Nayfeh, C. O. Chui, and K. C. Saraswat, Appl. Phys. Lett. **85**, 2815 (2004).

[67] Ge layers transfer to Si for photovoltaic applications, J. M. Zahler, C.-G. Ahn, S. Zaghi, H. A. Atwater, C. Chu, and P. Iles, Thin Solid Films 403-404, 558 (2002).

[68] Effect of mismatch strain on band gap in III-V semiconductors, C. P. Kuo, S. K. Vong, R. M. Cohen, and G. B. Stringfellow, J. Appl. Phys. **57** (12) 1985.

[69] J. K. Miller, To be published.

[70] R. Menzel, *Photonics: Linear and Nonlinear Interactions of Laser Light and Matter*, Springer, 2001.